Sensitivity of trefoil vortex knot reconnection to the initial vorticity profile

Robert M. Kerr[*]

Department of Mathematics, University of Warwick, Coventry CV4 7AL, United Kingdom

Five sets of Navier-Stokes trefoil vortex knots in $(2\pi)^3$ domains show how the shape of their initial profiles, Gaussian/Lamb-Oseen or algebraic, and their widths influence their evolution, as defined by their enstrophy $Z(t)$, helicity $\mathcal{H}(t)$, and changes in their dissipation-scale structures. Significant differences develop even when all have the same three-fold symmetric trajectory, the same initial circulation and the same range of the viscosities ν. The focus is upon how the dynamics of helicity density $h = \boldsymbol{u} \cdot \boldsymbol{\omega}$ affects reconnection and the evolution of enstrophy. $h \lesssim 0$ patches on the vorticity isosurfaces show where and how reconnection forms. For the Lamb-Oseen profile, the tightest and most linearly unstable, there is only a brief spurt of enstrophy growth as thin braids form at these positions; before being dissipated as the post-reconnection helicity $\mathcal{H}$ grows significantly. For the algebraic cases: as $h < 0$ vortex sheets form prior to reconnection, there is ν-independent convergence of $\sqrt{\nu}Z(t)$ at a common t_x. For those with the broadest wings, enstrophy growth accelerates after reconnection, leading to approximately convergent dissipation rates $\epsilon = \nu Z(t)$. Maps of terms from the budget equations onto centerlines illustrate the divergent behavior. Lamb-Oseen briefly forms six locations of centerline convergence with local negative dips in the helicity dissipation ϵ_h and vortical-helicity flux h_f. These are the source of the following positive increase in the global $\mathcal{H}$ and suppression of enstrophy production. For the algebraic profiles there are only three locations of centerline convergence, each with spans of less localized $\epsilon_h < 0$ that could be the seeds for the $h < 0$ vortex sheets and whose interactions can explain the later accelerated growth of the enstrophy, approximate ν-independent convergence of the energy dissipation rates ϵ, and evidence for finite-time energy dissipation ΔE_ϵ, despite the initial symmetries.

I. BACKGROUND

For the incompressible, three-dimensional Navier-Stokes equation the three significant quadratic integrated diagnostics of the velocity u and vorticity ω are: the kinetic energy with $E \sim 0.5u^2$; the enstrophy with $Z \sim \omega^2$; and the helicity $\mathcal{H}$. $\mathcal{H}$ is the global integral of the helicity density $h = \boldsymbol{u} \cdot \boldsymbol{\omega}$ and can take either sign. Equations representing their budgets are defined in Sec. II.

The robust relationship between the energy E and enstrophy Z is well-known. Given a viscosity ν, the energy dissipation rate $dE/dt = -\epsilon$ with $\epsilon = \nu Z$. The importance of ϵ for turbulent flows is that irregularity of the vorticity can lead to very large enstrophy and an energy dissipation rate ϵ that is large enough to support a finite Reynolds number-independent energy dissipation. This is known
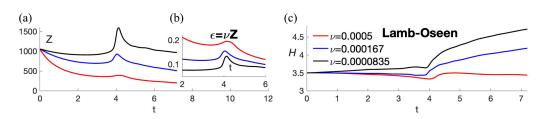
---

[*]Robert.Kerr@warwick.ac.uk

FIG. 1. Global diagnostics of a three-fold symmetric trefoil for case Gd05 with a Gaussian/Lamb-Oseen profile (10). The three Reynolds numbers are [2000, 6000, 12 000], with their viscosities in the legend. The diagnostics are the evolution of: (a) the enstrophy $Z(t)$, (b) the dissipation rate $\epsilon(t) = \nu Z$, and (c) the global helicity $\mathcal{H}(t)$. These are similar to Fig. 3 of Ref. [3]. All calculations are in $(2\pi)^3$ periodic boxes.

as a *dissipation anomaly*, defined as the finite integral

$$\Delta E_\epsilon = \int_0^{T_\epsilon} \epsilon \, dt > 0 \quad \text{in a finite-time } T_\epsilon. \tag{1}$$

This is observed in many laboratory and environmental turbulent flows. This relation between irregular vorticity and turbulent decay is robust, but has this caveat: Can a smooth initial state far from boundaries numerically generate $\nu \to 0$ finite ΔE_ϵ without either forcing or a parameterized dissipation rate ϵ?

Could a better understanding of the helicity density h help? What is known is that without viscosity, for the inviscid $\nu = 0$ Euler equations, the global helicity $\mathcal{H}$ is preserved, in addition to the energy E. On that basis it has been proposed that $\mathcal{H}$ can constrain nonlinear Euler growth of the enstrophy Z. However, could the formation of local $h < 0$ along a vortex lead to a alternative scenario?

Trefoil vortex knots are an initial state that is inherently helical, self-reconnecting, and mathematically compact, meaning that they can be isolated far from boundaries. The goal of this paper is to revisit recent trefoil knots simulations [1–4] to ascertain why different initial vorticity profiles generate starkly contrasting answers to those questions.

Before the results in Refs. [1–4], the most that numerics has been able to tell us about the role of helicity is that for single-signed helical Fourier modes, energy dissipation can be suppressed for a short time [5]. These flows then evolve into traditional decaying numerical turbulence: without any further insight into whether h has a role in either achieving, or suppressing, finite energy dissipation as the viscosity decreases.

Could trefoil vortex knots robustly overcome those limitations? With robustly meaning, are the numerics adequate to reach consistent conclusions? One conclusion coming from comparing the recent trefoil papers is that the results are not robust. With different initial states or numerics, different trends are observed for the evolution of the enstrophy $Z(t)$ and helicity $\mathcal{H}(t)$, particularly as reconnection begins and immediately afterward.

To illustrate the differences, Figs. 1 and 2 compare the $Z(t)$ and $\mathcal{H}(t)$ evolution of two sets of calculations with the same circulation $\Gamma = 1$ (7) and same three-fold symmetric trajectories, but representing these initial core profiles: respectively, evolution using a Gaussian/Lamb-Oseen (10) core profile [3] and that of a $p_r = 1$ algebraic (9) core profile [2]. How do $Z(t)$ and $\mathcal{H}(t)$ evolve for these cases?

While the divergence of their $Z(t)$ and $\mathcal{H}(t)$ is modest before reconnection begins at $t_r \sim 4$, afterwards it is significant. For Lamb-Oseen the helicity $\mathcal{H}(t)$ grows significantly while the enstrophy $Z(t)$ decays. For the algebraic profile the enstrophy grows significantly, as seen previously [2]. Is there any foreshadowing of this divergence before then?

Going back to very early times, for both calculations $Z(t)$ decreases, meaning more enstrophy dissipation than production. This similarity between the two continues only until $t = 0.4$, after which $Z(t)$ and $\mathcal{H}(t)$ diverge slowly until the innermost (centerline) vorticity isosurfaces begin
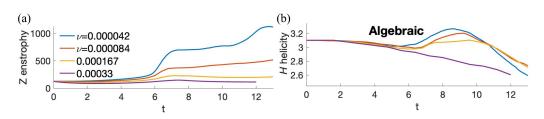
FIG. 2. Global diagnostics for algebraic case r1d015 whose profile (9) uses $p_r = 1$, $r_o = 0.015$ and $r_e = 0.08$. The Reynolds numbers are [24 000, 12 000, 6000, 3000], with their viscosities in the legend. Diagnostics are the evolution of: (a) the enstrophy $Z(t)$ and (b) the global helicity $\mathcal{H}(t)$.

to reconnect at a common time of $t_r \approx 4$. Then as $t \to t_r$, the differences become dramatic. For Lamb-Oseen, after some enstrophy growth at $t \sim t_r$, its enstrophy $Z(t)$ decreases again while the helicity $\mathcal{H}$ grows, with thin vortex bridges and braids forming, as previously observed [3] and discussed in Sec. III C.

In contrast, for the three-fold symmetric trefoils with a $p_r = 1$ algebraic profile, while reconnection begins at the same t_r, it is not completed until a somewhat later time of t_x. Figure 3(a) defines t_x as when there is ν-independent convergence of $\sqrt{\nu}Z(t)$, a "reconnection-enstrophy," convergence that has previously been associated with the formation of vortex sheets [2]. Figure 16 in Sec. III B goes further: showing that the vortex sheets have $h < 0$.

However, convergence of $\sqrt{\nu}Z(t)$ is not convergence of the dissipation rates $\epsilon(t) = \nu Z(t)$. What has been found for algebraic trefoils with perturbations, in far larger domains, is that convergence of $\epsilon(t) = \nu Z(t)$ in a finite time is possible [2]. Can the algebraic calculations reported here develop finite-time convergence of $\epsilon(t) = \nu Z(t)$: despite the three-fold symmetry and a tighter domain?

They do, with Fig. 3(b) providing evidence for weak convergence of the dissipation rates $\epsilon(t) = \nu Z(t)$ at $t_\epsilon \approx 2t_x$. In Fig. 2 this is accompanied by a modest increase in $\mathcal{H}(t)$ at the higher Reynolds numbers before $\mathcal{H}$ decays. This is discussed in Sec. III D.

To complete the discussion of profiles, a set calculations using the $p_r = 2$ Rosenhead regularized profile (9) of a point vorticity [6] is discussed in Sec. III F. The mathematics community calls this the Kaufman-Sculley profile, designated here as the K-S-R profile. The shape of the central core is intermediate between the two others, but its overall behavior is closer to that of the $p_r = 1$ algebraic profile.

Given these differences in the $Z(t)$ and $\mathcal{H}(t)$ evolution, these questions can be asked (tentative answers in parentheses).

(a) Can the $t \sim 0$ origins of the divergent behavior be identified? (The Rayleigh inflection-point instability discussed in Sec. II B.)

(b) What are the differences in the post-reconnection $t > t_x$ dissipative structures? (Sheets lead to a *dissipation anomaly*, braids and bridges do not.)
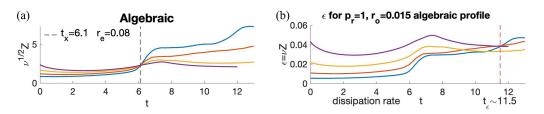

FIG. 3. For the case and viscosities from Fig. 2, two rescaled enstrophy diagnostics. (a) The time dependence of the reconnection-enstrophy $\sqrt{\nu}Z(t)$, with convergence at $t_x = 6.1$ indicated. This is used later to define the end of the first reconnection. (b) The dissipation rate $\epsilon(t) = \nu Z$, whose convergence at $t \approx 11$ might be preliminary evidence for the formation of a dissipation anomaly ΔE_ϵ. (1).
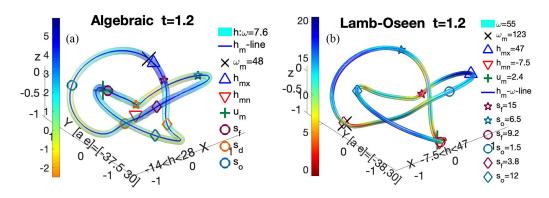
FIG. 4. Three-dimensional vorticity isosurfaces with mapped helicity at $t = 1.2$ for the two primary three-fold symmetric trefoils, both for $\nu \sim 8.4 \times 10^{-5}$. (a) From algebraic case r1d015 with $p_r = 1$ and $r_o = 0.015$ (9). (b) Lamb-Oseen profile (10) (Gd05). The primary extrema of interest are the maximum vorticity ω_m, the helicity minima h_{mn}, its maxima h_{mx}, and the maximum velocity u_m. All are indicated in both panels by the symbols in the legends. In addition, each panel indicates the three-dimensional s_f positions of the local centerline minima of the vortical helicity flux $\min(h_f)$ (6), as defined on budget profiles such as Fig. 9. Also shown are the s_f's opposing s_o points, the closest points in three dimensions on their opposite loops. Also indicated in panel (a) are the s_d positions of the local $\min(\epsilon_h)$, the minima of the centerline helicity dissipation. These positions are also marked on the $t = 1.2$ centerline budget profiles in Figs. 9 and 11 and will be used for reference later.

(c) Are there diagnostics for identifying the intervening, divergent $0 < t < t_r$ dynamics? (Mapping terms in the enstrophy and helicity budgets onto vortices' centerlines.)

To reduce the number of possible sources for those differences, all of the calculations here are three-fold symmetric and run in $(2\pi)^3$ periodic domains. This ensures that the only differences between each set of trefoils are the choices of their initial vorticity profiles and their widths.

Figure 4 provides an early time, three-dimensional perspective on the vorticity isosurfaces at $t = 1.2$ for algebraic case r1d015 and Lamb-Oseen Gd05. In terms of the overall structure they are almost identical. Perhaps the only identifiable difference is the different positions of the maximum of vorticity $\omega_m = \|\omega\|_\infty$, indicated by **X**. For the algebraic case on the left, ω_m is colocated with the blue triangle, the maximum of helicity h_{mx}. For Lamb-Oseen on the right, ω_m is at the maroon diamond, a local minima of the helicity flux (6), $\min(h_f)$. However, on the centerlines their respective enstrophy and helicity density budgets are quite different.

The paper is organized as follows. After the introduction of the profile-dependent evolution of the primary global diagnostics, and their early vorticity isosurfaces, the governing and budget equations are given. Next are the steps required to initialize the vortices, including how the raw, unbalanced mapped vorticity fields are made incompressible. Once the initial profiles are defined, recent mathematics for determining their stability is referenced and a set of diagnostics are introduced that map the terms from the enstrophy and helicity budget equations (5) and (6) onto the evolving centerline trajectories. Up to $t = 3.6$, both helicity-mapped vorticity isosurfaces and mapped centerline budgets are used in the comparisons between the evolution of cases Gd05 (Gaussian/Lamb-Oseen) and r1d015 ($p_r = 1$, $r_o = 0.015$ algebraic). The $t < t_r = 4$ differences in the budget terms lead to profound differences in the $t \gtrsim 4$ dissipative structures and dissipation rates $\epsilon(t)$. For Lamb-Oseen at and after reconnection: thin bridges, then braids and decaying dissipation rates. In contrast, for all of the algebraic calculations vortex sheets start to form with $\sqrt{\nu}Z(t)$ convergence for $t_x \lesssim 1.5t_r$; and for the widest initial algebraic profiles, the vortex sheets begin to wrap around one another at $t_x = 6$, leading to later ν-independent dissipation rates ϵ that approximately converge at $t_\epsilon \approx 2.5t_r \approx 10$.

II. EQUATIONS, NUMERICS, INITIAL CONDITIONS, CENTERLINE MAPS, STABILITY

The governing equations are the incompressible Navier-Stokes equations: for the velocity

$$\frac{\partial \boldsymbol{u}}{\partial t} + (\boldsymbol{u} \cdot \boldsymbol{\nabla})\boldsymbol{u} = -\boldsymbol{\nabla} p + \underbrace{\nu \triangle \boldsymbol{u}}_{\text{viscous drag}} \quad, \quad \boldsymbol{\nabla} \cdot \boldsymbol{u} = 0 \,; \tag{2}$$

and the vorticity $\boldsymbol{\omega} = \boldsymbol{\nabla} \times \boldsymbol{u}$

$$\frac{\partial \boldsymbol{\omega}}{\partial t} + (\boldsymbol{u} \cdot \boldsymbol{\nabla})\boldsymbol{\omega} = (\boldsymbol{\omega} \cdot \boldsymbol{\nabla})\boldsymbol{u} + \nu \triangle \boldsymbol{\omega}, \quad \boldsymbol{\nabla} \cdot \boldsymbol{\omega} = 0. \tag{3}$$

Numerics. All of the calculations are done in $(2\pi)^3$ periodic boxes with a two-thirds dealiased pseudo-spectral code and a high-wave number cutoff filter [8,11]. These features remove aliasing errors and absorb high-wave number fluctuations that would otherwise be reflected (in Fourier space) from the abrupt high-wave number cut-off. Extensive tests showed that with these features the calculations do at least as well as a calculation on a mesh that is 1.5 times greater. Some tests, such as doubling the mesh and comparing the maximum vorticities, have been repeated here.

Based on this past experience, the evolution of the global helicity and enstrophy shown for all cases can be trusted. For the more detailed analysis on vortex lines and three-dimensional graphics, the algebraic r1d015 $\nu = 1.6e\text{-}4$ statistics are reliable for all times, but those with $\nu = 8.4e\text{-}5$ are given only to $t = 3.6$. The detailed results for case Gd05 $\nu = 8.4e\text{-}4$ can be trusted up to $t = 4.4$, but not for $t \geqslant 4.8$.

Five initial profiles are discussed, each run for at least three viscosities. A larger number of profiles were done before choosing these five, so in the interest of economy and ease of use, the vorticity graphics for cases other than Gd05 and r1d015 use 512^3 meshes. Several of the smallest viscosity calculations, and all of the Lamb-Oseen calculations, are from 1024^3 mesh calculations.

The continuum equations for the densities of the energy, enstrophy and helicity, $e = \frac{1}{2}|\boldsymbol{u}|^2$, $\zeta = |\boldsymbol{\omega}|^2$ and $h = \boldsymbol{u} \cdot \boldsymbol{\omega}$, with their production, flux and dissipation rates are the following:

$$\frac{\partial e}{\partial t} + (\boldsymbol{u} \cdot \boldsymbol{\nabla})e = -\boldsymbol{\nabla} \cdot (\boldsymbol{u}p) + \nu \triangle e - \underbrace{\nu(\boldsymbol{\nabla}\boldsymbol{u})^2}_{\epsilon = \text{dissipation} = \nu Z} \quad, \quad E = \frac{1}{2} \int \boldsymbol{u}^2 dV \,; \tag{4}$$

$$\frac{\partial \zeta}{\partial t} + (\boldsymbol{u} \cdot \boldsymbol{\nabla})|\boldsymbol{\omega}|^2 = \underbrace{2\boldsymbol{\omega} S \boldsymbol{\omega}}_{\zeta_p = \text{production}} + \nu \triangle |\boldsymbol{\omega}|^2 - \underbrace{2\nu(\boldsymbol{\nabla}\boldsymbol{\omega})^2}_{\epsilon_\omega = Z-\text{dissipation}} \quad, \quad Z = \int \boldsymbol{\omega}^2 dV \,; \tag{5}$$

$$\frac{\partial h}{\partial t} + (\boldsymbol{u} \cdot \boldsymbol{\nabla})h = \underbrace{-\boldsymbol{\omega} \cdot \boldsymbol{\nabla}\Pi}_{h_f = \omega-\text{transport}} + \underbrace{\nu \triangle h}_{\nu-\text{transport}} - \underbrace{2\nu \text{tr}(\boldsymbol{\nabla}\boldsymbol{\omega} \cdot \boldsymbol{\nabla}\boldsymbol{u}^T)}_{\epsilon_h = \mathcal{H}-\text{dissipation}} \quad \mathcal{H} = \int \boldsymbol{u} \cdot \boldsymbol{\omega} dV. \tag{6}$$

$\Pi = p - \frac{1}{2}\boldsymbol{u}^2 \neq p_h$ is not the pressure head $p_h = p + \frac{1}{2}\boldsymbol{u}^2$.

While the global energy E and helicity $\mathcal{H}$ are inviscid invariants [10], their inviscid Lagrangian local densities e and h can change due to the pressure gradient $-\boldsymbol{\nabla} p$ and the ω-transport h_f, respectively. Under $\nu \neq 0$ Navier-Stokes, both the helicity flux h_f and dissipation ϵ_h can generate local negative helicity $h < 0$. Note that h is not locally Galilean invariant due to h_f.

Is there a role for the helicity density $h < 0$? In particular, can local $h < 0$ break helicity's constraint upon the nonlinear growth of the enstrophy Z? Section II D shows how this question can be addressed by mapping the budget terms onto the vorticity centerlines.

For short times another set of inviscid short-time conservation laws are the circulations Γ_i for closed loops $\mathcal{C}_i$ about those trajectories:

$$\Gamma_i = \oint_{\mathcal{C}_i} \boldsymbol{u}_i \cdot \boldsymbol{r}_i, \quad \text{where} \quad \boldsymbol{r}_i \text{ is a closed loop about } \mathcal{C}_i. \tag{7}$$

With the appropriate choice of the closed loop, Γ_i can be preserved during Navier-Stokes reconnection for very short times. Could this constraint that have additional consequences?

A. Initial conditions

Four elements are used to define an incompressible vortex knot.

(1) The $x(\phi)$ trajectory of the centerline of the vortex knot (8).

(2) The vorticity profiles $|\omega(\rho)|$, with the distance ρ defined as the distance between a given mesh point x and the nearest point on the trajectory $x(\phi)$: $\rho = |x - x(\phi)|$.

(a) The profiles are either algebraic (9), with a chosen power-law p_r, or Gaussian/Lamb-Oseen (10).

(b) Each $|\omega(\rho)|$ has two parameters: A radius r_o and the centerline vorticity ω_o. These control the initial circulation $\Gamma(0)$.

(c) $\Gamma(0)$ was determined empirically by integrating and averaging $\omega_\perp$ across four planes, x-z or y-z. The procedure was validated using the Lamb-Oseen case, for which Γ can be determined analytically.

(d) In this paper $\Gamma(0) = 1$ and $r_f = 1$ are fixed so the nonlinear timescale for all the calculations is $t_{\mathrm{NL}} = 1$ (8).

(e) The final ω_o are chosen so that the circulation $\Gamma \equiv 1$ (7) after step 4.

(3) The chosen profile is mapped onto a Cartesian mesh using previous algorithms [1], with the direction of vorticity given by the centerline direction: $\hat{\omega}(\rho) = \hat{\omega}(x(\phi))$.

(4) Finally, we need to remove the nonsolenoidal components of the raw vorticity field by projection. This also makes the velocity field incompressible. Except for the Lamb-Oseen profile, this operation invariably leads to reductions in the values of the maximum vorticity ω_m and the enstrophy Z.

The initial trajectory $\boldsymbol{\xi}_0(\phi) = [x(\phi), y(\phi), z(\phi)]$ of all the trefoils in this paper is defined over $\phi = 1 : 4\pi$ by this closed double loop, with $a = 0.5$, $w = 1.5$ $r_f = 1$ and $r_1 = 0$:

$$x(\phi) = r(\phi)\cos(\alpha)$$

$$y(\phi) = r(\phi)\sin(\alpha) \quad z(\phi) = a\cos(\alpha)$$

$$\text{where} \quad r(\phi) = r_f + r_1 a \cos(\phi) + a\sin(w\phi + \phi_0)$$

$$\text{and} \quad \alpha = \phi + a\cos(w\phi + \phi_0)/(wr_f)$$

$$\text{with} \quad t_{\mathrm{NL}} = r_f^2/\Gamma \text{ the nonlinear timescale,}$$

$$\text{and} \quad r_e = [\Gamma/(\pi\omega_m)]^{1/2} \text{ the effective radius.} \tag{8}$$

The four algebraic Rosenhead regularized profiles $\omega_{\mathrm{raw}}(\rho)$ are parameterized by a radius r_o, maximum/centerline vorticity ω_o and a power law p_r,

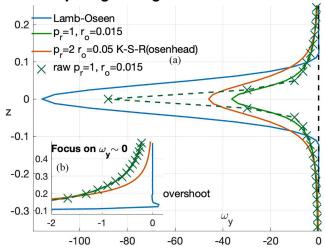$$\omega_{\mathrm{raw}}(\rho) = \omega_o \frac{(r_o^2)^{p_r}}{(\rho^2 + r_o^2)^{p_r}}. \tag{9}$$

For a columnar vortex, Eq. (14) suggests that the $p_r = 2$ K-S-R profile is stable unless there are perturbations with high azimuthal wave number m (13). The "broader" $p_r = 1$ algebraic profile has been used as the second initialization step of several earlier papers [1,2,9].

The Gaussian/Lamb-Oseen profile is

$$\omega_{\mathrm{raw}}(\rho) = \omega_o \exp(-(\rho/r_o)^2) \quad \text{for} \quad \rho < \rho_+. \tag{10}$$

This definition of the Lamb-Oseen profile has these advantages: $\omega_m = \omega_o$ and the effective radius $r_e = r_o$, without the factor of 2 required by the Lamb-Oseen profile in current use [3]. The only difference between that profile and (10) is that the core in Fig. 5 below is $\sqrt{2}$ wider. This, along with a different definition of the enstrophy Z (5) (a factor of 2), yields enstrophy and helicity evolution that are (in appearance) nearly identical to theirs [3].

Table I gives the details of the five initial profiles: The parameters r_o and ω_o for the profile formulas (9) and (10) and the generated raw enstrophies Z_o. Then the divergence-free $t = 0$ values

FIG. 5. Comparisons of $\omega_y(z)$ at $t = 0$ between vortices initialized with algebraic and Lamb-Oseen core profiles. The $\omega_y(z)$ profiles are taken through the $\min(\omega_y)$ of the $y = 0$ x-z planes as in Figs. 7 and 8. Three cases from Table I are used. All except one curve are taken after the nonsolenoidal Fourier components have been removed. The profiles are for the $r_o = 0.05$ Lamb-Oseen case (10) (Gd05) and two of the algebraic profiles that use the Rosenhead regularization (9). r2d05: $p_r = 2$, $r_o = 0.05$, referred to as K-S-R, and r1d015: $p_r = 1$, $r_o = 0.015$. The other curve is the "raw" $p_r = 1$, $r_o = 0.015$ curve, taken through its pre-Fourier-projected ω_y field. (a) The primary figure shows the full profiles in z. (b) The lower-left inset focuses upon $z < 0.4$ wings with small ω_y. Note the slight $\omega_y > 0$ overshoot at the boundaries of the Lamb-Oseen profile. This is the likely seed for the oscillations about $\omega_y = 0$ in Fig. 8.

are given: the effective radii r_e (8), vorticity maxima ω_m, and enstrophies $Z(0)$. The viscosities are given in the figure legends.

An additional, inherent parameter is the maximum radius ρ_+ used to map $\omega_{\mathrm{raw}}(\rho)$ onto the Cartesian mesh in step 3. Empirically, the trefoils' evolution is independent of ρ_+ so long as the circulation $\Gamma = 1$ and $\rho_+ \sim 0.5 - 1$ (trefoil radius is $r_f = 1$), with $\rho_+ \geqslant 0.75$ for all cases here.

The specific profiles listed are: Lamb-Oseen (case Gd05), two broad algebraic $p_r = 1$ cases (r1d015, r1d006) and two K-S-R $p_r = 2$ cases (r2d05, r2d1). With most of the analysis figures are taken from the highest Reynolds number calculations of the Lamb-Oseen (Gd05) and the $p_r = 1$,

TABLE I. Raw core radius r_o and vorticity ω_o parameters, resulting enstrophy Z_o, then effective radii $r_e(8)$, maximum vorticity ω_m and enstrophy Z after fields are made divergent-free. The $t_{3D-\omega}$ column is the last time for which detailed three-dimensional graphics were made for those cases. The global enstrophy $Z(t)$ and helicity $\mathcal{H}(t)$ are reliable for all cases listed. The only Lamb-Oseen case is labeled Gd05 and the algebraic cases are labeled by the power-law p_r as in r1d015: (r1$\equiv p_r = 1$) and raw core radii (d015$\equiv r_o = 0.015$).

Cases	p_r	n^3	r_o	ω_o	Z_o	r_e	ω_m	$Z(0)$	ν's	$t_{3D-\omega}$
Gd05	−	1024^3	0.05	130	1057	0.05	130	1055	5×10^{-4} 1.67×10^{-4} 8.35×10^{-5}	$t \leqslant 4.4$
r2d05	2	512^3	0.05	64.3	326	0.07	62	306	3.3×10^{-4} 1.67×10^{-4} 8.4×10^{-5}	$t \leqslant 5.2$
r2d1	2	512^3	0.1	17.85	97.1	0.14	17.3	96.5	3.3×10^{-4} 1.67×10^{-4} 8.4×10^{-5}	All times
r1d006	1	1024^3	0.006	554	333	0.053	138	229	1.67×10^{-4} 8.4×10^{-5}	Only $Z, \mathcal{H}$
r1d015	1	1024^3	0.015	100	138	0.078	56	124	1.67×10^{-4}	$t \leqslant 6$
r1d015	1	512^3	0.015	100	138	0.078	56	124	3.3×10^{-4} 4.2×10^{-5}	Only $Z, \mathcal{H}$
r1d015	1	1024^3	0.015	100	138	0.078	56	124	8.4×10^{-5}	$t \leqslant 3.6$

$r_o = 0.015$ "broad" algebraic profile (r1d015). Figure 4 compares their slightly evolved $t = 1.2$ three-dimensional helicity-mapped vorticity isosurfaces.

Figure 5 compares the $t = 0$ profiles of $\omega_y(z)$ for three of the profiles in Table I. Each is taken through the $\min(\omega_y)$ positions in their $y = 0$, x-z planes, as in Fig. 7 below. Both the main figure[†] and the "wings" inset show that all of the $t = 0$ algebraic profiles have smooth extended wings that never overshoot the $\omega_y = 0$ axis. In contrast, on the outer edge of the Lamb-Oseen profile there is some overshoot, consistent with what has been seen before when Gaussian-like profiles are used for antiparallel reconnection [7,11].

The source of the Lamb-Oseen overshoot arises from the combined effects of the steepness of the outer edge of the L-O profile and a limitation of the algorithm (here and [3]) that is used to map the $\omega_{\text{raw}}(\rho)$ field onto the Cartesian mesh in step 3. The mapping problem arises when the directions $\hat{\omega}$ of neighboring mesh points come from different positions on the centerline, a problem that is common when the distance ρ from the centerline is large. The steepness problem arises when finite $|\omega|$ points are next to points with $|\omega| \approx 0$. The mapped field sees these as finite jumps. Combined, in step 4 the projection of the mapped field can generate overshoots to negative values on the profile's edge, overshoots whose magnitude is a function of the curvature of the centerline and the outer, $\rho \sim \rho^+$, steepness of $|\omega|(\rho)$.

To demonstrate the importance of excessive steepness, one can decrease the maximum radius ρ^+ on an otherwise smooth profile. For a $\rho_+ = 0.025$ variant of the $p_r = 1$, $r_o = 0.015$ the evolution of $Z(t)$ and $\mathcal{H}(t)$ changed from evolution similar to that in Figs. 2 and 3 to evolution more like that of Lamb-Oseen in Fig. 1. The implications of this could be the topic of another paper.

B. Rayleigh stability criterion

The stability of different core profiles $\omega(\rho)$ can be determined using the $J(\rho)$ (12) stability functions. The $J(\rho)$ are a type of Richardson number and derived for columnar vortices [12] by extending an earlier result for shears on boundary layers.

Recent analysis [13] that determines and uses the $J(\rho)$ begins with the azimuthal profiles of the velocity $u(\rho)$, vorticity $\omega(\rho)$, and the pressure p:

$$u = V(\rho)e_\theta, \quad \omega = W(\rho)e_z, \quad p = P(\rho). \tag{11}$$

P is determined up to an additive constant by centrifugal balance $rP'(\rho) = V^2(\rho)$. Then by introducing the angular velocity $\Omega(\rho) = V(\rho)/\rho$ and $\Phi(\rho) = 2\Omega(\rho)W(\rho) = -P$, one can define these $\mathcal{C}^\infty$ and $\mathcal{C}^1$ functions:

$$\Phi(\rho) = 2\Omega(\rho)\omega(\rho) \quad \text{and} \quad J(\rho) = \frac{\Phi(\rho)}{\Omega'(\rho)^2}, \quad \rho > 0. \tag{12}$$

Next, consider a small, but not tiny, perturbation of one Fourier mode:

$$\boldsymbol{u}(\rho, \theta, z, t) = u_{m,k}(\rho, t)e^{im\theta}e^{ikz}, \quad \boldsymbol{\omega}(\rho, \theta, z, t) = \omega_{m,k}(\rho, t)e^{im\theta}e^{ikz}, \tag{13}$$

stability is determined by

$$\frac{k^2}{m^2}J(\rho) \geqslant \frac{1}{4} \quad \text{for all} \quad \rho > 0. \tag{14}$$

Figure 6 shows $J(\rho)$, and how it is determined, for the Lamb-Oseen (10) and $p_r = 2$ algebraic (9) profiles for the same $\omega_o = 1$ and $r_o = 1$. What is important are their different $\rho \to \infty$ behavior. For the Lamb-Oseen profile,

$$J_G(\rho) \to \frac{\rho^4}{r_o^2}e^{-(\rho/r_o)^2} \to 0, \tag{15}$$

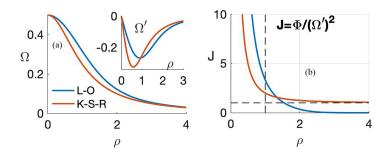implying that the inequality (14) is always violated as $r \to \infty$.

FIG. 6. Stability at $t = 0$ of the Lamb-Oseen (L-O) (10) and K-S-R (9) profiles using the Richardson functions $J(\rho)$ (12) of Howard-Gupta [12] in two steps. (a) First, because each profile uses $r_o = 1$ for their width, their $\Omega(\rho)$ and $\Omega'(\rho)$ profiles are similar. (b) However, what determines stability is how their $J(\rho)$ asymptote as $\rho \to \infty$. For Lamb-Oseen its $J(\rho) \to 0$ (15), suggesting instability, while K-S-R is almost always stable because, by (14), $J(\rho) \to r_o^2$ is finite.

Whereas for the K-S-R $p_r = 2$ algebraic profile,

$$\frac{k^2}{m^2}J(\rho) \to \frac{\left(k^2 r_o^2\right)}{m^2} \quad \text{as} \quad \rho \to \infty. \tag{16}$$

This says that unless m is large for $k r_o \sim 1$, that is its azimuthal wavelength is small, then for all ρ, $(k^2/m^2)J(\rho) \geqslant \frac{1}{4}$ can be satisfied. An example of a small perturbation is the Lamb-Oseen perturbation in the inset of Fig. 5, probably generated by the solenoidal projection in initialization step 4 in Sec. II A.

Can the respective algebraic and Lamb-Oseen $J(\rho)$ stability curves in Fig. 6 foretell whether their evolution diverges at early times? The first test in Figs. 7 (r1d015, $t = 2.4$) and 8 (Gd05 $t = 1.2$). considers vertical profiles of ω_y taken though $y = 0$, x-z slices.

For K-S-R, $J(\rho) \to r_o^2 > 0$, so stability is expected if m is large, as demonstrated by the ω_y contours in Fig. 7. For Lamb-Oseen $J(\rho) \to 0$ ($< \frac{1}{4}$) and because there is a small perturbation, instability is possible. This is demonstrated by the irregular $\omega_y \sim 0$ contours in Fig. 8. What is less clear for Lamb-Oseen is how tiny the perturbations must be to create instability [13], as discussed in Sec. IV B.
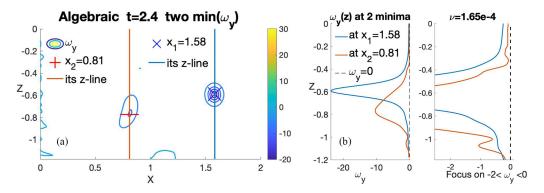

FIG. 7. From algebraic case r1d015 at $t = 2.4$, a $y = 0$ ω_y $x-z$ cross section with $\omega_y(z)$ profiles through the local $\min(\omega_y)$ indicated. (a) Contour plot whose primary $\min(\omega_y)$ is at $x_1 = 1.58$ with a secondary minima at $x_2 = 0.81$. $|\omega_y| \sim 0$ contours do not appear. (b) $\omega_y(z)$ profiles through those local minima. First, the full $\omega_y(z)$, then focusing on small ω_y. Contours and profiles at $t = 1.2$ are similar.
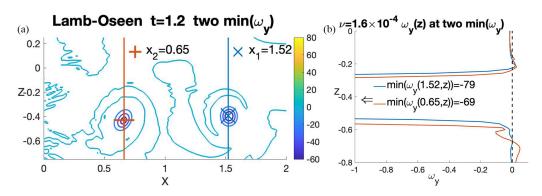
FIG. 8. From the Lamb-Oseen (10) case Gd05 at $t = 1.2$, a $y = 0$ ω_y $x-z$ cross section with $\omega_y(z)$ profiles through the local min(ω_y) indicated. (a) Contour plot whose primary min(ω_y) is at $x_1 = 1.52$ with a secondary minima at $x_2 = 0.65$. A few $|\omega_y| \sim 0.001$ contours are included to show the fluctuations about $\omega_y = 0$. (b) $\omega_y(z)$ profiles through those local minima. Values of the negative min($\omega_y(z)$) are indicated. The positive overshoots of $\omega_y(z)$ show the magnitude of the $|\omega_y| \sim 0$ contours on the left. Note that the $y = 0$, $x-z$ plane negative ω_y extrema are not at the positions of the global max($|\omega|$) for these fields.

C. Effect of being stable or unstable

Do the stability differences indicated by Figs. 6–8 yield differences in the subsequent evolution of the Lamb-Oseen and algebraic cases?

One difference between the respective x-z slices (Figs. 7 and 8) is that the algebraic contours in Figs. 7 do not generate oppositely signed contours. In contrast, Lamb-Oseen in Fig. 8 does: as shown by the $|\omega_y| \sim 0$ contours and the $\omega_y(z)$ slice on the right. These fluctuations of oppositely signed ω_y are a source of local interactions, interactions that could be the source for the $t = 1.2$ differences between the algebraic and Lamb-Oseen centerline budget profiles in Figs. 9 and 11, respectively. This is discussed further in Sec. III A.

D. Mapping budgets terms onto centerline vortices

While single-color helicity isosurfaces [1] suggested that helicity has a role in reconnection, the mapped h-vorticity isosurfaces used by two 2021 trefoil papers [3,4] are a better tool. In particular, small values of localized oppositely signed helicity $h < 0$ indicated where reconnection was forming.

There are similar yellow to red $h < 0$ patches at $t = 1.2$ in Fig. 4, for both algebraic and Lamb-Oseen. For all cases, up to $t = 3.6$ there are similar $h < 0$ patches on their inner, higher ω isosurfaces. However, are the observed $t \leqslant 3.6$ differences sufficient for identifying the origins of the post-reconnection differences in the evolution of the algebraic and Lamb-Oseen calculations? Given how small those $t \leqslant 3.6$ inner isosurface differences are, they are not. Why are the surface helicities of the different cases qualitatively similar? This is likely because before reconnection begins, similar long-range Biot-Savart terms dominate the surface helicity dynamics for all cases. Therefore, what is needed are new diagnostics related to what is within the isosurfaces to explain the major differences in the $T > 3.6$ enstrophy and helicity evolution in Figs. 1 and 2, meaning that another set of pre-reconnection diagnostics is required.

Because these are questions about the evolution of local helicity $h(\boldsymbol{x}, t)$, which is controlled by its budget equation (6), one alternative set of diagnostics is to instead map the primary terms from the enstrophy and helicity density budget equations (5) and (6) onto the isosurfaces. The variations of these terms upon the isosurfaces are very small and are not useful for analyzing the dynamics by themselves. However, this exercise indicated that the local variations are strongest near the centerlines.
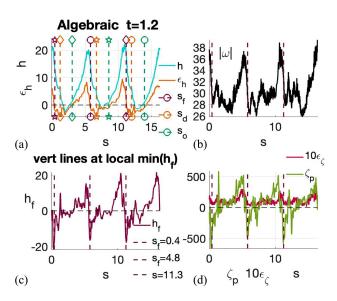
FIG. 9. Centerline budget profiles at $t = 1.2$ for algebraic case r1d015 $\nu = 1.6 \times 10^{-4}$ of h, ϵ_h, $|\omega|$, h_f, ϵ_ζ and ζ_p. (a) h and ϵ_h (6). (b) $|\omega|$. (c) h_f. (d) Enstrophy density production ζ_p and its dissipation rate ϵ_ζ (5). Each panel has three vertical maroon lines at the s_f positions of the local min(h_f). Panel (a) has two additional sets: s_d positions of the local min(ϵ_h); s_o positions that oppose the s_f. All of the $0.4 < t \lesssim 2.4$ algebraic budget profiles are similar to these.

This suggests that a better way to visualize the budget terms would be to map them onto the vorticity centerlines directly, if the centerlines can be identified. If successful, then this would provide us with an analysis tool that is both local (at a point) and global (between distant points on the centerline).

To identify centerlines one must first choose appropriate seed points $\boldsymbol{x}_\omega(0)$ within a vorticity isosurface, then trace the vortex lines emanating from those points using a streamline function, giving trajectories $\boldsymbol{x}_\omega \in \mathcal{C}$ obeying

$$\boldsymbol{\xi}_\omega(s) = \frac{d\boldsymbol{x}_\omega(s)}{ds} = \boldsymbol{\omega}(\boldsymbol{x}_\omega(s)), \text{ whose lengths are } L_\omega = \oint |\boldsymbol{\xi}_\omega(s)| ds. \tag{17}$$

In Refs. [2,9] the position of the maximum vorticity was used as the seed. With more experience, it has been found that seeding at either maximum or minimum of helicity, then using $-\boldsymbol{\omega}(\boldsymbol{x})$ direction in Eq. (17), yields trajectories that stay within the observed isosurfaces. This is the practice in this paper.

In all cases, the trajectories do not close upon themselves perfectly, which is only relevant for determining the topological numbers, twist, helicity, and self-linking as in earlier work [2,9]. That is not an objective of this paper.

Once the trajectories have been defined, the profiles of important dynamical terms are mapped onto those curves to determine how those properties are related to one another.

Note that because these vortex lines are almost closed upon themselves, initially the integral of the stretching $u_{s,s} = d\boldsymbol{u}/ds \cdot \hat{\omega}$ on the ω-line is identically zero:

$$\oint_0^{L_\omega} u_{s,s} ds = u(L_\omega) - u(0) \equiv 0. \tag{18}$$

Due to this, any stretching along this line at $t = 0$ is balanced by equal compression somewhere else. For these vortices, that compression also immediately yields an increase in the local enstrophy dissipation and negative helicity dissipation rates, ϵ_ζ and $-\epsilon_h$, as well as a very early decrease
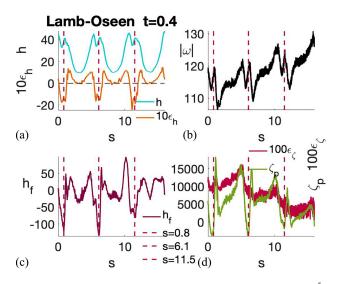
FIG. 10. Early $t = 0.4$ Lamb-Oseen centerline budget profiles for $\nu = 8.35 \times 10^{-5}$, $r_o = 0.05$ of h, ϵ_h, $|\omega|$, h_f, ϵ_ζ, and ζ_p. These are similar, but not identical, to the algebraic profiles at $t = 1.2$ in Fig. 9. From panel (c), the three s_f positions of local $\min(h_f)$ are colocated with: (a) local $\max(h)$ and $\min(\epsilon_h)$; (b) secondary local max $|\omega|$; (d) local $\min(\zeta_p)$, meaning at points of maximum centerline compression.

in the enstrophy and increase in the helicity: $dZ/dt|_{t=0} < 0$ and $d\mathcal{H}/dt|_{t=0} > 0$ as seen in Fig. 1 (Lamb-Oseen) and Fig. 2 (algebraic), more for the larger ν Lamb-Oseen calculations than the others.

E. Using these tools as time progresses

The six terms from enstrophy and helicity budget terms that are mapped onto the centerlines are arranged into four panels:

(a) The helicity density h (cyan) and its dissipation rate ϵ_h (yellow).
(b) The vorticity magnitude $|\omega| = \sqrt{\zeta}$ (black).
(c) Helicity flux h_f (maroon), which includes a pressure gradient.
(d) Enstrophy density dissipation ϵ_ζ (red) and production ζ_p (lime).

These six mapped terms are teamed with relevant three-dimensional helicity-mapped vorticity isosurfaces, all of which indicate the locations of the primary extrema in three-dimensional space:

$\omega_m = \|\omega\|_\infty$ **X** (black); $h_{mx} = \max(h)$ △ (blue); $h_{mn} = \min(h)$ ▽ (red); $u_m\max(u)$ + (green). Their closest points on the centerlines are shown on the budget profiles, particularly on $h(s)$ in panel (a).

Also shown in some figures are the following global minima and maxima:

$\zeta_{p-mx} = \max(\zeta_p)$ ◁ (jungle-green); $\zeta_{p-mn} = \min(\zeta_p)$ ▷ (red-orange); $\epsilon_{\zeta-mx} = \max(\epsilon_\zeta)]$ ∗ (violet-red); $h_{f-mn} = \min(h_f) = \min(h_f)$ □ (maroon).

All four panels appear in Figs. 9, 10, 14, and 18. For Fig. 11 (Gd05, $t = 1.2$), Fig. 12 (Gd05, $t = 2.4$), and Fig. 15 (r1d015, $t = 3.6$), some panels are not shown. In particular, panel (b) with $|\omega|$ is not shown because its s-profile closely follows that for the helicity h.

To identify relationships between the budget terms on the four panels, sets of three-fold symmetric dashed vertical lines are added at significant positions to allow comparisons between panels. The choice of vertical lines changes over time. At early times when transport along the vortices is most important, the local extrema of negative helicity transport $\min(h_f)$ positions are the best. Later, as reconnection begins, the local minima of the helicity dissipation $\min(\epsilon_h)$ are best. The notation, symbols and colors of the local extrema with vertical lines are:

(a) *Maroon s_f* indicates the positions of the local $\min(h_f)$ with these symbols:
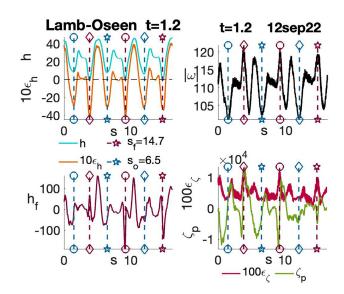
FIG. 11. Lamb-Oseen centerline budget profiles at $t = 1.2$ for $r_o = 0.05$, $\nu = 8.35 \times 10^{-5}$. These are very different than the $t = 1.2$ algebraic budget profiles in Fig. 9. In panel (a) there are six positions with strong negative helicity dissipation, local $\min(\epsilon_h)$ and local $\min(h)$. The positions are separated into two sets of three. The s_f in maroon are at the strongest $\min(\epsilon_h)$, adjacent to the local $\min(h_f)$ (h_f panel is not shown). The s_o in turquoise are the points that oppose the s_f in three dimensions (Fig. 4). In panel (b), all six positions are at very large positive gradients of ζ_p between local $\min(\zeta_p)$ and $\max(\zeta_p)$. Strong local $\min(\zeta_p)$ means strong local centerline compression. The s_f are also at $\max(\epsilon_\zeta)$ positions, maxima of the enstrophy dissipation.
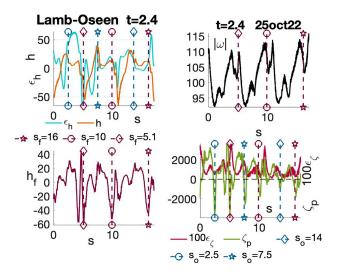

FIG. 12. Lamb-Oseen centerline budget profiles at $t = 2.4$ for $r_o = 0.05$, $\nu = 8.35 \times 10^{-5}$. (a) $h(s)$, $\epsilon_h(s)$, s_f (maroon) for local $\min(h_f)$ and the s_f's opposing s_o (turquoise) are marked. The $\epsilon_h(s)$ profiles are three-fold symmetric again and more like the algebraic profiles at $t = 1.2$ and $t = 2.4$ and Lamb-Oseen at $t = 0.4$. (b) However, there are still six positions of local $\min(\zeta_p) < 0$ compression: The three s_f and three s_o. Having this many local compression locations is why the post-reconnection Lamb-Oseen vortex structures in Sec. III C are braids, not the sheets generated by the algebraic profiles.
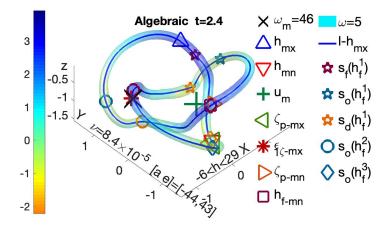
FIG. 13. Algebraic mapped-helicity ω-isosurface at $t = 2.4$ from the r1d015 $p_r = 1$ (9), $\nu = 8.4 \times 10^{-5}$ calculation at the beginning of the initial phase of reconnection. Symbols (from legend) show the three-dimensional positions of the basic u, ω, and h extrema as well as the extrema of terms taken from the enstrophy and helicity budget equations (5) and (6). Also shown, taken from the next figure, are the three-dimensional locations of these centerline positions: the s_f (maroon) positions of local $\min(h_f)$; the s_o (turquoise) positions that oppose the s_f; and the s_d (yellow) positions of the local $\min(\epsilon_h)$. The s_f points are on one side of each reconnection, with the s_d-s_o zones representing the other side of those reconnections. The best diagnostic for following the Biot-Savart evolution of the vortex centerlines from $t = 1.2$ to 3.6 is the convergence within each of the three color-coded clusters of $\circ$'s, $\star$'s and $\diamond$'s. These clusters, plus the extrema appearing with them, are: a $\circ$ cluster on the left with ω_m (**X**), $\max(\epsilon_\zeta)$; a $\star$ cluster above u_m (green **+**) near the global $\min(h_f)$ (maroon square) and $\min(\zeta_p)$; and a $\diamond$ cluster at the bottom with $\min(h)$ and $\max(\zeta_p)$. Over time, the s_d and s_o with the same symbols are approaching one another on the same centerline spans of the trefoil and together they approach the s_f in three-dimensions.

    (i) $\star$ star,
    (ii) $\diamond$ diamond,
    (iii) $\circ$ circle.

(b) *Yellow* The s_d positions for local $\min(\epsilon_h)$ are important when reconnection is, or will be, forming.

(c) *Turquoise* is used for the s_o/s_o^+ positions opposing (min or max=+) extrema of the helicity flux h_f, meaning the points that oppose in three-dimensions the s_f/s_f^+, respectively. Each s_o/s_o^+ is separated from its s_f/s_f^+-position by approximately $\Delta s = L_\omega/2$ along the centerline, where $L_\omega/2$ is half the length of the centerline trajectory (17).

(d) *Green* is for the three-fold s_g points opposing the s_d local $\min(\epsilon_h)$ points.

At specific times:

(1) For algebraic case r1d015:

    (a) At $t = 2.4$ in Figs. 13 and 14 the $s_o(h_f)$ that oppose the s_f are near s_d with local $\min(\epsilon_h)$.

    (b) For transitional $t = 3.6$ in Fig. 15, s_f and s_d are equally important as they mark the opposite sides of each developing reconnection site.

    (c) For $t = 4.8$, representing $t > 4$, the s_d and s_g mark where there is active reconnection.

(2) For *Lamb-Oseen*

    (a) For $t = 1.2$ and 2.4 in Figs. 11 and 12 the s_f and s_o mark where reconnection will form.

    (b) For $t = 3.6$ in Figs. 18 and 17(a), reconnections are marked by pairs of local s_f^+ (in cobalt) and s_o^+ points, while the s_d and s_f are colocated and far from the active reconnection between the s_f^+ and s_o^+.

These budget maps show the dynamical interplay between the enstrophy and helicity over the period leading to reconnection for the broadest $p_r = 1$ algebraic case r1d015 and Lamb-Oseen case
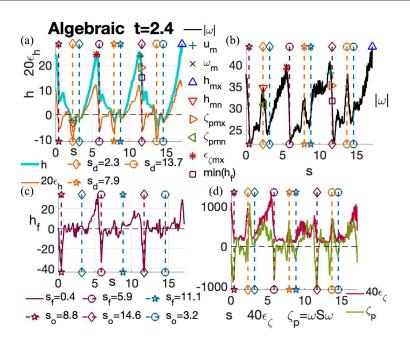
FIG. 14. Algebraic centerline budget profiles at $t = 2.4$ of h, ϵ_h, $|\omega|$, h_f, ϵ_ζ, and ζ_p, for case r1d015, $\nu = 8.4 \times 10^{-5}$. Added to each panel are three sets of three dashed vertical lines. Maroon lines are at the s_f of local min(h_f). Yellow is for the s_d at local min(ϵ_h). And turquoise is for the s_o, the points opposing the s_f in three-dimensions. The s_f points are on one side of each reconnection, with of the s_d-s_o zones representing the other side of those reconnections. Over time, the s_d and s_o with the same symbols are approaching one another on the same centerline spans of the trefoil.

Gd05. For the K-S-R, $p_r = 2$ cases in Sec. III F, only the essential time evolution and mapped helicity isosurfaces are given.

III. RESULTS

The comparisons between helicity-mapped vorticity isosurfaces and the mapped centerline budget terms are presented chronologically:

III-A Early times for algebraic ($t = 1.2$) and Lamb-Oseen ($t = 0.4, 1.2, 2.4$).

III-B Algebraic mid-reconnection at t=2.4 and $t = 3.6$, with the first appearance of extended $h < 0$ vortex sheets. After $t = 3.6$, the algebraic and Lamb-Oseen vortical structures and global evolution of $Z(t)$ and $\mathcal{H}(t)$ diverge, as shown by Figs. 1 and 2.

III-C $t \geqslant 3.6$ Lamb-Oseen Gd05. There is reconnection with vorticity bridges and localized sheets at $t = 4$ in Fig. 19, then with braids at $t = 4.4$ in Fig. 20.

III-D $t = 4.8$ algebraic mid-reconnection with broad $h < 0$ ω-sheets.

III-E $t \sim 6$ algebraic reconnection how broad vortex sheets lead to wrapping and accelerated enstrophy growth.

III-F Finally there is a short discussion of the K-S-R $p_r = 2$ r2d05 case.

A. Early times ($t = 0.4, 1.2,$ one Lamb-Oseen $t = 2.4$) profile-dependent evolution and differences

To begin, recall that for the $t = 1.2$ isosurfaces in Fig. 4 (cases r1d015, Gd05), the only clear difference between the panels is the position of the vorticity maximum ω_m. Can the centerline budget maps identify any greater differences at early times? First, the similarities at very early times are given, then the differences.
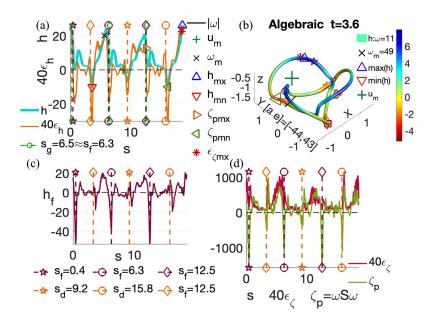
FIG. 15. Algebraic centerline budget profiles and an isosurface at $t = 3.6$ for case r1d015 for $\nu = 8.4 \times 10^{-5}$. Budget profiles: h, ϵ_h, h_f, ϵ_ζ, and ζ_p, with added vertical dashed lines in each panel for these local positions: s_f [maroon, min(h_f)], s_d [yellow, min(ϵ_h)], and in the upper-left panel with s_g (green) for the s_d opposing points. The s_f are also at min(ζ_p) and are at two of the max(ϵ_ζ) positions, local enstrophy dissipation peaks. The s_d are also at the local minima of the helicity min(h) < 0, at crossovers between secondary local min(ζ_p) to max(ζ_p) and at two of the local max(ϵ_ζ) positions. They are colocated with the opposing positions to the s_f. The s_g oppose the s_d and are nearly coincide with the s_f. Where might reconnection form? The positioning of the s_f and s_d, plus their opposing points, suggests that reconnection is forming between the s_f and s_d. Panel (d) shows that at all six points there is local $\zeta_p < 0$, that is $du_s/ds < 0$. Due to incompressibility this implies the existence of stretching perpendicular to the vorticity at these points, the stretching needed to needed to create the $h < 0$ vortex sheets. The large vorticity ($\omega = 0.2\omega_m$) isosurface in the upper-right panel encases the centerline and includes centerline symbols from panel (a), with the labels for the auxiliary symbols given in Fig. 16. This isosurface also shows continuity with the earlier evolution of its inner isosurfaces.

The centerline maps for the corresponding earliest times in Fig. 9, $t = 1.2$ algebraic, and Fig. 10, $t = 0.4$ Lamb-Oseen, are similar. While the strongest local max(h) and local max($|\omega|$) are near to one another, other local extrema are associated with local min(h_f), the vortical helicity flux indicated by dashed maroon lines at local s_f. Positions of local helicity dissipation minima (min(ϵ_h) < 0) are near the s_f and the positions of local compression, min(ζ_p) < 0 are on the s_f. This suggests that the dominant dynamics at these points is local compression with pinching at these points on the vortices.

However, starting at $t = 1.2$ the centerline dynamics of the two profiles diverge.

(1) For *algebraic case r1d015*, the alignments in Fig. 9 persist from $t = 0.4$ until the reconnection time of $t_r \sim 4$ is approached.

(2) However, for *Lamb-Oseen* at $t = 1.2$, the corresponding Lamb-Oseen budgets in Fig. 11 are very different, showing six locations with roughly equivalent variations of the positive and negative helicity dissipation ϵ_h at six significant local min(h_f) positions, split into two sets of three, maroon s_f and turquoise s_o.

In Fig. 11(a) the s_f positions at local min(h_f) < 0 (not shown) are also at the largest dips of $h \sim 0$ and the strongest local min(ϵ_h). In Fig. 11(b), the s_f are not exactly on local min(ζ_p), but on the adjacent large positive gradients and local enstrophy dissipation peaks: max(ϵ_ζ). These s_f can be viewed as one side of the developing reconnection sites.

The turquoise s_o positions that oppose the s_f positions in Fig. 4 are the other side of the developing reconnections. They are also secondary local $\min(\epsilon_h)$, secondary local dips in h and near secondary local $\min(\zeta_p)$, meaning that all six positions (the s_f and s_o) are sitting at or near local compressive $\min(\zeta_p) < 0$.

Having multiple points of local compression at an early time has a significant effect upon the the enstrophy growth (or decay). At $t = 1.2$ and 2.4, the localized pinching enhances the localized dissipation of both helicity ϵ_h and enstrophy ϵ_ζ, which also suppresses the ζ_p terms needed to enhance enstrophy growth: before that growth has even begun. A likely source of this localization of the dynamics is the interactions between the primary vorticity and the oppositely signed flotsam seen in Fig. 8. That is, the origin of this localized dynamics is the amplification of that noise by instability, as previously suggested [7] and discussed here in Sec. II B.

The $t = 2.4$ Lamb-Oseen centerline budget profiles in Fig. 12 show some return to normal. They have similarities with the $t = 0.4$ Lamb-Oseen profiles in Fig. 10 and the pre-reconnection algebraic profiles for $t \leqslant 3.6$. While there are only three local $\min(\epsilon_h)$ and $\min(h_f)$, in the right panel there still is strong compression with local $\min(\zeta_p) < 0$ at all six of the former ($t = 1.2$) $\min(h_f)$ positions: The three current ($t = 2.4$) s_f positions and their three s_o opposing positions. In addition, the magnitudes of the enstrophy production ζ_p and dissipation ϵ_ζ terms are tempered, being a factor of 5 less than at $t = 1.2$.

This localized dynamics is only temporarily stronger than the long-range Biot-Savart interactions: Once that dynamics dissipates, the Biot-Savart interactions again control the large scales and the evolution of the centerline trajectory. However, the dynamics along the centerlines is permanently affected. When reconnection bridges do form, with some enstrophy growth, it is entirely concentrated at the locations in Fig. 11, but not over the entire trefoil, with rapid post-reconnection dissipation of the vorticity in the bridges, leading to divergent evolution of the enstrophy $Z(t)$ and the helicity $\mathcal{H}(t)$. This is explained further in Sec. III C.

B. Mid-reconnection $t = 2.4, 3.6$, with algebraic spawning sheets

In the $t \leqslant 3.6$ period before reconnection begins, there are few differences between the inner, larger ω isosurfaces of cases r1d015 and Gd05. However, there are significant differences between their pre-reconnection budget profiles, significant enough that for this mid-reconnection phase, the evolution of algebraic case r1d015 and that of Lamb-Oseen case Gd05 are considered separately. The primary algebraic case in this section and Lamb-Oseen in Sec. III C.

To follow the evolution of the r1d015 isosurfaces and budgets between $t = 1.2, 2.4$, and 3.6, three sets of symmetric positions are indicated on each: s_f at local $\min(h_f)$; the s_d at local $\min(\epsilon_h)$; and points opposing either the s_f (the s_o) or the s_d (the s_g). These are in addition to the usual extrema: $\max |u|$, $\max |\omega|$, $\max(h)$, $\min(h)$, $\min(\epsilon_h)$, $\min(h_f)$, $\max(\epsilon_\zeta)$, and the min and $\max(\zeta_p)$. Once defined, the s_f, s_d, and s_o/s_g can be used to follow the evolution of the isosurfaces and budget profiles of the r1d015 calculation as follows:

(a) *Evolution* between the times $t = 1.2, 2.4$, and 3.6:

(i) The isosurfaces are drawn together in three-dimensions between the s_f and s_o points of closest approach.

(ii) At the same time, the s_d and s_o approach one another along the centerline until they coincide at $t = 3.6$ ($s_o \approx s_d$).

(iii) On the centerlines the s_f are next to secondary local $\min(\epsilon_h)$, starting at $t = 2.4$ and more strongly at $t = 3.6$.

(iv) At $t = 2.4$ and 3.6 there are secondary local $\min(\epsilon_h) < 0$ next to the s_f. On both the isosurfaces and the centerlines as in Figs. 13, 14(a), 15(a), and 15(b). With some $h \lesssim 0$ at the s_d.

(b) Diagnostics that indicate a $t = 3.6$ transition.

(i) At the s_d besides $s_o \approx s_d$, in Fig. 15(a) there are deepening local $\min(h) < 0$. The strongest red-orange on the isosurface in Fig. 15(b) comes from these local $\min(h) < 0$. Also in Fig. 15(c), at the s_d there are secondary local $\min(h_f)$ and in Fig. 15(d) there are secondary local $\min(\zeta_p)$.
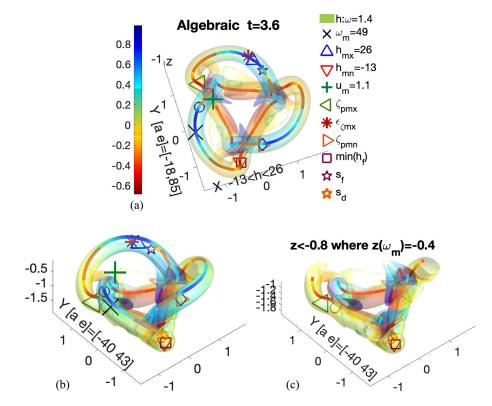
FIG. 16. Algebraic $t = 3.6$ mapped helicity, ω-isosurface from three-perspectives for case r1d015 with $\nu = 8.35 \times 10^{-5}$, with a color-coded centerline. Symbols show the three-dimensional positions of the basic u, ω, and h extrema as well as extrema from the enstrophy and helicity budget equations (5) and (6). Also, the s_f (maroon) positions of local $\min(h_f)$ and the s_d (yellow) positions of the local $\min(\epsilon_h)$, which also oppose the s_f (the s_o in Fig. 15). Panel (a) is a plan view perspective with faint $h \lesssim 0$ yellow sheets extending out from the lower reddish ring and panels (b) and (c) are side views from the same perspective. Panel (b) shows the entire domain. Panel (c) shows only $z < -0.8$ with the yellow lower ring emerging below the blue, largely $h > 0$, upper portion. In panels (b) and (c) the $\star$ $s_d = 9.2$ mark is enlarged. The centerline vortex has mapped helicity ranging from red ($h = -13$) to blue ($h = 26$). By using a small $\omega \sim 1.4 \sim 0.03\omega_m$ vorticity isosurface, a gradation can be seen in the lower $h < 0$ zone from a red $h \sim -0.4$ inward facing half to the yellow-green $h \lesssim 0$ outward half. This is the first step in the formation of the yellow negative helicity $h \lesssim 0$ vortex sheets at later times.

(ii) This, together with the primary local $\min(\zeta_p)$ colocated with the s_f in Fig. 15(d), means that there is pinching at each end of where the innermost portions of the trefoil loops will touch. However, unlike Lamb-Oseen in Sec. III C, this does not lead to braids.

(iii) This is because at the same time in Fig. 15(b), there are growing spans of $\epsilon_h \lesssim 0$ yellow-green on the isosurface between the leading s_d points and the following s_f. For example, on the centerlines, between the yellow $\star$ at $s_d = 9.2$ and the maroon $\circ$ at $s_f = 6.3$.

(iv) These small patches of $h < 0$ and $\epsilon_h < 0$ on the centerline spans in Fig. 15(a) and inner isosurface are not by themselves evidence for $h < 0$ vortex sheets. Instead, the patches of $\epsilon_h \lesssim 0$ could be evidence of where $h < 0$ vortex structures are being created. More complete $t = 3.6$ isosurfaces are given next and by Fig. 28 in the Appendix.

(c) What is new in Fig. 16 at $t = 3.6$ is extensive $h < 0$ on a small ω, outer isosurface, with red for strong $h < 0$ along the red-coded centerline in the lower ($z < -0.8$) portion of the trefoil, with

both red ($h < 0$) and yellow ($h \lesssim 0$) patches on the isosurfaces and faint signs of where vorticity is being shed.

(i) All the s_d and red centerline patches are on the lower ($z < -0.7$) part of the isosurfaces, emphasized most strongly in Fig. 16(c). The reddish $h < 0$ patches extend over roughly two-thirds of the s_f-s_d spans noted in Fig. 15(b),

(ii) The $s_f = 6.3 \circ$ to $s_d = 9.3 \star$ span noted before shows the relation between the reddish inner side of the surface to the centerline. The transition from the the reddish zones smoothly into the yellowish, more sheetlike outer surfaces is seen best in Fig. 16(a).

(iii) This is a trend continues to later times, as illustrated at $t = 4.8$ below by the red and yellow patches in Figs. 21–23.

C. Gaussian/Lamb-Oseen reconnection: Braid formation

In Sec. III A early divergence of $t = 1.2$ Lamb-Oseen budget profiles from the algebraic profiles was shown, respectively, in Fig. 11 (Gd05) and Fig. 9 (r1d015). This section shows the effect of that early divergent dynamics upon Lamb-Oseen as reconnection begins, beginning at $t = 3.6$ with Figs. 17 and 18. $t = 3.6$ is the last time that a single centerline could be identified for case Gd05.

The Lamb-Oseen analysis ends with the $t = 4$ and 4.4 isosurfaces in Figs. 19 and 20. These show how the trefoil then breaks into two vortex rings, connected first by what could be described as bridges, then as braids.

The two $t = 3.6$ isosurfaces in Fig. 17 are the following:

(a) A primary, higher magnitude $\omega = 19$ isosurface that shows continuity with the earlier Biot-Savart evolution and has minimal differences with the $t = 3.6$ inner algebraic structure in Fig. 15.

(b) The lower magnitude $\omega = 1.7$ isosurface shows how the Lamb-Oseen profile reconnection begins on the outer wings, with sheets shedding with some $h \lesssim 0$. These sheets with bits of $h \leqslant 0$ are localized around the reconnection points, unlike the broad $h < 0$ isosurface zones of the r1d015 algebraic trefoil in Fig. 16.

The $t = 3.6$ budget profiles and isosurfaces in Figs. 17 and 18 have three sets of primary local positional marks. The s_d, s_f^+, and s_o^+ markers, plus the s_f:

(i) The s_d in yellow (with embedded maroon s_f) are at local $\min(\epsilon_h) + \min(h_f)$ positions. The s_d are exactly on local $\max(|\omega|)$ and $\max(\epsilon_\zeta)$, the maximum enstrophy dissipation.

(ii) The s_f^+ in cobalt are at the local $\max(h_f)$ and are coincident with local $\max(\zeta_p)$. Local $\zeta_p > 0$ implies stretching, suggesting that these positions could be the seeds for the bridges that form during reconnection.

(iii) The third set of s_o^+ in turquoise are at the points opposing the s_f^+. The s_o^+ are also local $\min(h)$ and $\min(\zeta_p)$, local compression, suggesting that there is pinching on the trefoil vortex at the other end of the nascent bridges.

(iv) All consistent with active reconnection at these positions.

After $t = 3.6$ the trefoil splits into two rings.

(a) What can the $t = 3.6$ markers tell us about how this separation forms.

(i) The cobalt $\max(h_f)$ s_f^+ points with large $\zeta_p > 0$ become one end of the bridges, with their opposing turquoise s_o^+ at the other end.

(ii) The s_d yellow $\min(\epsilon_h)$ points are on what becomes the upper (u) ring, with magnitudes $h_u > 0$.

(iii) The turquoise $s_o^+/\min(h)$ points become the lower (ℓ) ring, with some $h(s_o^+) < 0$ appearing on the localized vortex sheets in Fig. 17(b), such as to the left of ω_m ($\mathbf{X}$).

(b) What develops out of this $t = 3.6$ state?

(i) At $t = 4$ in Fig. 19, short, flattened bridges are generated as the trefoil is begins to separate into two rings. The positions of ω_m, u_m, h_{mx}, and h_{mn} are all on the bridges.

(ii) At $t = 4.4$, in Fig. 20, the new upper (blue) and lower (red) rings are separating, with each bridge splitting into two braids. The positions of ω_m, h_{mx}, and h_{mn} are on the the lower ring and u_m is on the upper ring.
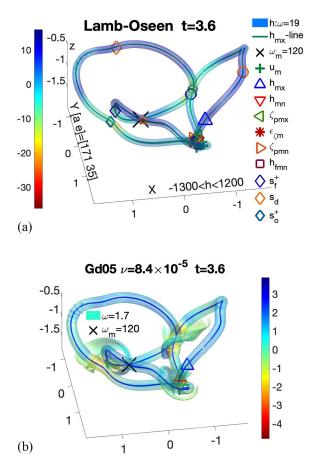
FIG. 17. Two $t = 3.6$ Lamb-Oseen isosurfaces with different vorticity thresholds. (a) The primary $\omega = 19$ isosurface is similar to the higher-ω algebraic isosurface in Fig. 15. Additional markers indicate the three-dimensional locations of the s_d (yellow), local min(ϵ_h), s_f^+ (cobalt) for the local max(h_f) points, and s_o^+ (turquoise), points opposing the s_f^+ that are also min$(h) < 0$ and min(ζ_p) points. Reconnection is commencing between the s_f^+ and s_o^+ points. The local s_d (yellow), min(ϵ_h) sit in strongly positive $h > 0$ zones, not $h < 0$ as for the algebraic calculations or Lamb-Oseen for $t \leqslant 2.4$. (b) The vorticity of the second isosurface uses very small $\omega = 1.7$ to show that the outer edges of the isosurface are shedding sheets with slightly negative helicity.

(c) Figs. 19 and 20 are roughly equivalent to the Re $= 12\,000$ figures at the same times for the previous trefoil calculations using Lamb-Oseen profiles [3]. Including the splitting of each bridge into two braids. So providing further Gaussian/Lamb-Oseen graphics and discussion in this paper is unnecessary.

The following summary using the Lamb-Oseen budget profiles in Figs. 11, 12, and 18 can help explain the Lamb-Oseen evolution of the global enstrophy $Z(t)$ and the helicity $\mathcal{H}(t)$ in Fig. 1:

(i) Starting at $t = 0$ when $\int ds \, \zeta_p \equiv 0$, for the spans with local compression, $\zeta_p < 0$, the viscous terms and ϵ_ζ are enhanced, resulting in $Z(t)$ decreasing for at least short $t \gtrsim 0$ times for all cases and viscosities ν.

(ii) Between $t = 2.4$ and 3.6, the global enstrophy production and its dissipation rate are approximately equal to their centerline integrals: $Z_p = \int dV \zeta_p \sim \int ds \, \Gamma \zeta_p$ and $\epsilon_Z = \int dV \epsilon_\zeta \sim \int ds \, \Gamma \epsilon_\zeta$.

(iii) With Z_p and ϵ_Z roughly balancing one another in Figs. 12 and 18 ($t = 2.4, 3.6$), giving $dZ/dt = Z_p - \epsilon_Z \approx 0$ over the temporal span of $2.4 \leqslant t \leqslant 3.6$, and relatively steady $Z(t)$, enstrophy, over those times in Fig. 1.
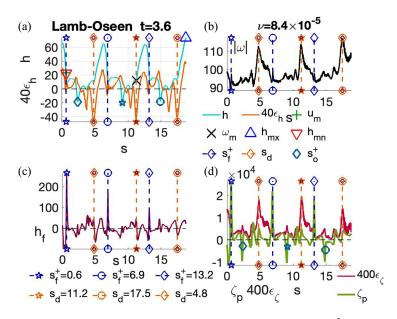
FIG. 18. Lamb-Oseen centerline budget profiles at $t = 3.6$ for $\nu = 8.35 \times 10^{-5}$. The s_d (yellow/maroon) at local $\min(\epsilon_h)$ and colocated with local $\max(\epsilon_\zeta)$ and $\max(|\omega|)$, are in large $h > 0$ zones far from the reconnections. The s_f^+ (cobalt) are at local $\max(h_f)$ points and colocated with local $\max(\zeta_p)$ and secondary velocity minima. The s_o^+ (turquoise) points oppose the s_f^+ and are colocated with $\min(h) < 0$ and $\min(\zeta_p)$ points. Reconnection is commencing between the s_f^+ and their opposing s_o^+ points.

(iv) At $t = 3.6$ in Fig. 18, at the locations of positive, not negative, spikes in h_f, there are sharp positive spikes in the enstrophy production ζ_p.

(v) These spikes of $\zeta_p > 0$ continue through $t = 4$, generating the brief enstrophy spurt in Fig. 1. This spurt is when the bridges form, shown in Figs. 17 and 19.

(vi) Then as the strong centerline enstrophy dissipation ϵ_ζ in Fig. 18 takes over, the centerline spikes of local $h_f > 0$, $\zeta_p > 0$ and $\omega = \sqrt{\zeta}$ and ζ_p, are dissipated, along with the temporal spikes of $Z(t)$ in Fig. 1.

(vii) For $\mathcal{H}(t)$, except at $t \sim 1.2$ as in Fig. 11, its $t \leqslant 3.6$ evolution is dominated by the strongly localized negative helicity dissipation ϵ_h, which removes $h < 0$, thereby leading to increasing $\mathcal{H}(t) > 0$. After $t = 3.6$, as dissipation removes the small amounts of $h < 0$ associated with the bridges, $\mathcal{H}(t)$ increases further.

D. Algebraic reconnection scaling with $h < 0$ ω-sheets

Due to the constraints imposed upon the calculations in this paper, a three-fold symmetry and the $(2\pi)^3$ periodic domain, it has been a surprise that the algebraic profile cases have generated this: Finite-time, finite energy dissipation ΔE_ϵ (1), as shown in Figs. 2 and 25 by the finite-time convergence of the dissipation rates $\epsilon(t) = \nu Z$ of the broadest profiles: cases r1d015 and r2d1. At least for a short range of viscosities. The evidence for finite ΔE_ϵ in the earlier perturbed trefoil calculations [2] could be achieved only by using very large domains.

Furthermore, for all of the algebraic profile calculations there are vortex sheets and convergent $\sqrt{\nu}Z$, such as in Fig. 3 (r1d015) and the examples in Sec. III F, although with profile-dependent convergent times $t_x > t_r$.

What are the underlying structures and dynamics that allow the subsequent enstrophy growth to accelerate and form finite ΔE_ϵ for these cases? Figures 15, 16, and 28 at $t = 3.6$ show where, and how, the conditions for generating negative helicity vortex sheets originate. This section extends
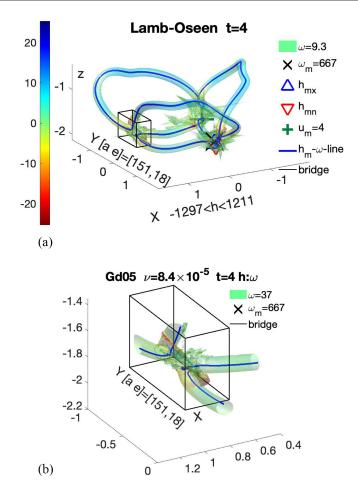
FIG. 19. Two Lamb-Oseen isosurfaces at $t = 4.0$. The panels are related to one another by an boxed-outline they share that contains a bridge. (a) The primary isosurface shows the overall structure using a small vorticity of $\omega = 9.3 = 0.014\omega_m$. There are the three symmetric locations of yellow-green $h \lesssim 0$ where the loops are interacting and forming bridges between the rings. Panel (b) shows a $\omega = 37$ isosurface that focuses upon the lower-left reconnection site to highlight one of the reconnection bridges. There is a noticeable $h < 0$ string within the bridge, but no $h < 0$ vortex sheets.

that analysis to $t = 4.8$ to show how the sheets then expand and contribute to the enstrophy growth: growth that can lead to finite-time energy dissipation. Skipping the gradual changes at the intermediate times of $t = 4$ and $t = 4.4$. The important differences with the Lamb-Oseen calculation are also highlighted.

The three-dimensional structure at $t = 4.8$ is illustrated in Figs. 21 and 22 using several perspectives of two vorticity isosurfaces and red $h < 0$ hash marks. Mapped h is on the broader isosurface with a lower vorticity, $\omega = 0.64 \approx 0.02\omega_m$, and a higher vorticity $\omega = 14$ blue isosurface that encases the centerline vortex. The red hash marks indicate $\epsilon_h \lesssim 0$ centerline spans from budgets in Fig. 23. Figure 21 shows the entire structure from two perspectives: a plan view and a side view.

To clearly see the yellow $h \lesssim 0$ sheets, Fig. 22 lops off upper parts of the trefoil, with perspectives from above and below. Without the $h > 0$ upper regions obscuring the lower region, it is easier to see that the reddish $h < 0$ vorticity is coming from the inner side of the trefoil centerline and the yellow vortex sheets are expanding from the outer side of the centerline. These observations are continuations of the trends noted at $t = 3.6$, with everything associated with $h \lesssim 0$ amplified.
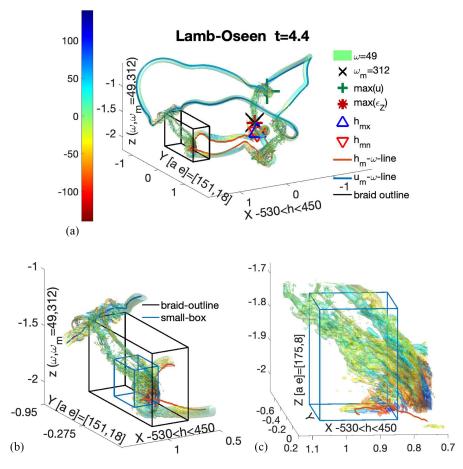
FIG. 20. Three views of a $t = 4.4$ Lamb-Oseen isosurface with $\omega = 49 = 0.015\omega_m(=312)$, with the bottom two focusing upon the smallest structures. (a) The primary $t = 4.4$ isosurface shows the overall structure to indicate how braids are forming from bridges, as seen for previous Lamb-Oseen calculations. Two vortex rings have formed whose centerline vortices are an upper ring with a blue centerline that was seeded by $u_m = \max(u)$ and a lower, red centerline that was seeded by $h_m = \max(h)$. (b) The full length of one of the double braids is shown, including where it attaches to the new upper and lower vortex rings. This is similar to $t = 4.29$ of Fig. 18 from Ref. [3]. (c) The small box at one end of the double braid shows it winding around the primary vortex.

The $t = 4.8$ budget profiles in Fig. 23 can tell us more about where and how $h \lesssim 0$ is being shed. It is the orange s_d that show where one side of active reconnection is forming, with their opposing points being the green s_g. The red hashes with consistent $\epsilon_h < 0$ run from to two-thirds the way from one s_d to the next s_d. For example from the orange $s_d \star$ towards the $\diamond s_d$.

The maroon s_f positions are no longer part of the ongoing reconnection, but are on a $h > 0$ zone that is becoming an upper vortex rings, while the red hashes and the s_d and s_g marks are becoming part of a lower ring. The side view in Fig. 21(b) shows this more clearly.

Further algebraic r1d015 remarks:

(i) In Fig. 23(a) the s_d mark the primary $\min(h) < 0$ positions and in Fig. 23(c) the positions of $\max(\epsilon_\zeta)$, enstrophy dissipation.

(ii) The $\epsilon_h \lesssim 0$ spans with red hashes show that the reconnection between the loops is between segments on those loops and is not simply point-to-point as with Lamb-Oseen.
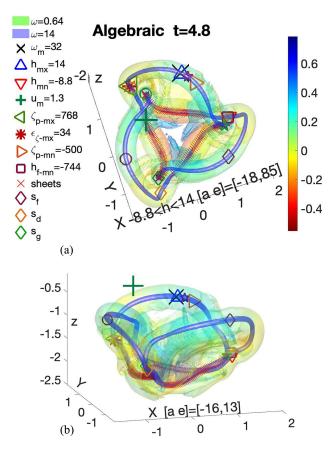
FIG. 21. Two views of the same $t = 4.8$ isosurface from different elevation angles from the $p_r = 1$, $r_o = 0.015$ (r1d015) calculation: (a) (planar view) and (b) (side view). The time of $t = 4.8 > t_r \sim 4$ represents the middle of the reconnection phase that ends with the first reconnection at $t_x = 6$. The ω-isosurfaces are: a blue inner $\omega = 14$ surface and a small $\omega = 0.65 = 0.02\omega_m$ isosurface with mapped helicity. The positions of ω_m, max(h), min(h), and u_m are given along with extrema of terms from the enstrophy and helicity budgets. The red hashes indicate where sheets arise from the marked centerline spans of $\epsilon_h < 0$ in budget [Fig. 23(a)], plus three triplets of the local positions s_f, s_d, and s_g at local min(h_f), min(ϵ_h), and the s_d opposing points. The symbols given in the legend are also used in Fig. 23. In panel (a) the overall structure of the lobes is emphasized. Panel (b) shows that the red hashes are all in the lower portion and represent where a separate lower vortex ring is forming. The origins and location of the yellow regions are given in the next figure.

(iii) The yellow vortex sheets at $t = 4.8$ now encompass almost the entire interior within the trefoil.

Lamb-Oseen and algebraic comparisons. In comparing algebraic Fig. 21 to Lamb-Oseen in Fig. 18, the only similarity is that reconnection is forming between a primary marker and its opposing point. However, the primary L-O reconnection markers are not the s_d, but the s_f^+ at local max(h_f) points, locations with stretching, $\zeta_p > 0$, not compression. This contributes to the dynamics responsible for why the algebraic and Lamb-Oseen reconnection structures are so different.

While Lamb-Oseen creates isolated braids that quickly dissipate, and shut down enstrophy production, the algebraic profiles shed vortex sheets, sheets whose mutual interactions can accelerate enstrophy production.

To demonstrate the full extent and nature of the vortex sheets, in Fig. 22 the upper, blue $h > 0$ zone has been lopped off, leaving the broad yellow vortex sheets around the lower vortex ring visible.
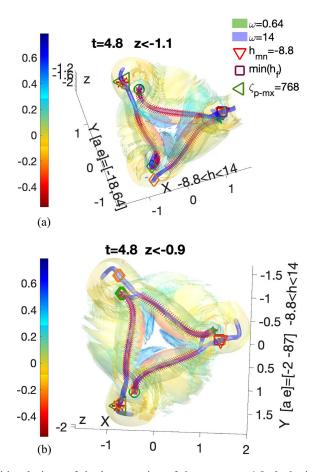
FIG. 22. Two additional views of the lower region of the same $t = 4.8$ algebraic isosurface as the last figure. The views show $z < -1.1$ and -0.65, respectively. Each perspective is dominated by yellow $h \lesssim 0$ with (a) looking down and (b) looking up with the domain flipped across a line from $[x\ y] = [-1\ 1.5]$ (green triangle) to the $[x\ y] = [1\ -1]$ corner, with some of the upper $h > 0$ zone included. It is also rotated a bit about the z axis to give a flavor of how the legs of the lower ring are connecting with the bridge. Gray is where we are looking through both the lower yellow and upper blue. Some of the $h > 0$ zone is included to show the while the $h \lesssim 0$ sheets are being shed from the lower $h < 0$ centerline, they extend up to the upper $h > 0$ blue-marked centerline. The orange s_d and the opposing green s_g, both marked with $\diamond$'s, are highlighted to show how the legs might be starting to wind around each other.

E. Later times: Centerline budgets and $t = 6$ impressions of bridge formation

Up through $t = 3.6$ the centerline budget profiles have largely been used to identify the origins of the divergent evolution between the two types of initial vorticity profiles. What can the $t \geqslant 3.6$ centerline budgets tell us about the dynamics and structures during the following phase?

First question: Why is so little negative helicity ($h < 0$) seen on the centerlines? That is, despite the presence of neighboring $h < 0$ vortex sheets.

A likely contributing factor is the spans of strong $\epsilon_h < 0$ on the centerlines that can act as sponges that remove newly created centerline $h < 0$.

Second question: What is the local dynamics when the trefoil starts to break into two rings? At $t = 3.6$, the three s_d and the opposing s_f-s_g are all at locations with local $\min(h_f)$ and $\min(\zeta_p)$, indicating local compression and pinching along the vortex lines on both sides of the developing
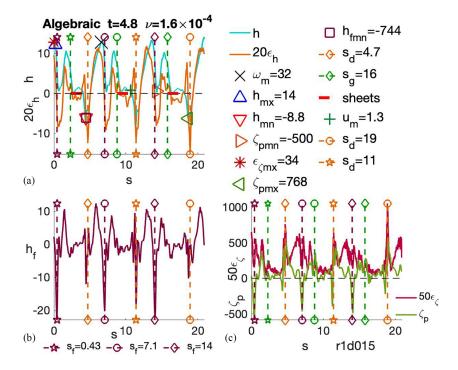
FIG. 23. Algebraic centerline budget profiles at $t = 4.8$ for case r1d015 with $\nu = 1.67 \times 10^{-4}$. Profiles: h, ϵ_h, h_f, ϵ_ζ, and ζ_p, with added vertical dashed lines for these local positions: s_f [maroon, $\min(h_f)$], s_d [yellow, $\min(\epsilon_h)$], and s_g (green) for the s_d opposing points. The s_f are also at $\min(\zeta_p)$ and at large local enstrophy dissipation ϵ_ζ positions. The s_d are at secondary $\min(\zeta_p)$ and at local $\max(\epsilon_\zeta)$ positions. The $\epsilon_h(s) \lesssim 0$ spans over which the $h < 0$ sheets are being shed are indicated by thick, dashed red lines that are to the right of each s_g. Reconnection is forming between spans near each s_d and the red hashed patches on the opposing loops with green s_g symbols at one end, for example, at the $s_d = 4.7$ yellow diamond at the other end and the span next to the green diamond at $s_g = 16$.

reconnection bridges. This is probably due in part to the interactions between the bridges' two ends in three-dimensions.

Third question: How long does this compression/pinch persist? At $t = 4.8$ in Fig. 23, the local $\min(h_f)$ and $\min(\zeta_p)$ diagnostics that foreshadowed reconnection for $t \leqslant 3.6$ still have coincident large negative spikes. However, these are now located within the developing upper ring, far from the three developing reconnections and, unlike at $t = 3.6$, are not adjacent to s-spans with significant enstrophy production, $\zeta_p > 0$.

Fourth question: Even as the compression/pinch dynamics subsides at $t \sim 4.8$, why does the enstrophy continues to grow? On the centerlines this is because the yellow, local $\min(\epsilon_h)$ s_d points still have local enstrophy production maxima, $\max(\zeta_p) > 0$. Overall, this is because for $t \geqslant 4.8$, most of the enstrophy production is coming from the growth of the $h < 0$ vortex sheets that that now envelop the lower ring and the bridges that connect the upper and lower rings.

Why is the creation of $h < 0$ sheets for $t \leqslant 4.8$ so important? There are these two reasons. First, by creating $h < 0$ zones, the vorticity in the $h > 0$ zones can grow; this breaks the early, nearly inviscid, helicity conservation constraint upon vorticity growth. Second, by spreading the vorticity into sheets, the enstrophy in Fig. 2 can continue to grow during the first phase of reconnection; unlike the Lamb-Oseen enstrophy in Fig. 1. The creation of the sheets sets up the next stage when those sheets begin to interact with one another at $t = 6$.
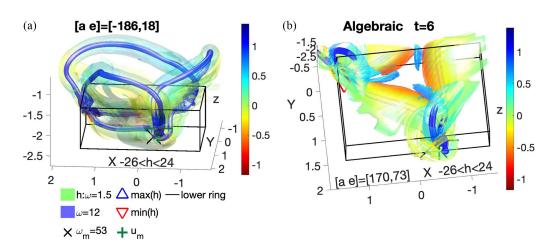
FIG. 24. Two isosurface perspectives ([a e]) at $t = t_x = 6$ for algebraic r1d015, $\nu = 1.6 \times 10^{-4}$, at the end of the first reconnection, as defined by Fig. 3(a). This is when the dissipation in Fig. 3(b) begins to accelerate, with convergence of $\epsilon = \nu Z$ at $t \approx 10$. The two isosurfaces are an inner $\omega = 12$ blue that encases the centerline and an outer $\omega = 15$ with helicity-mapping. The perspective angles [a e]=Ω_z [rotation elevation] are in the figures. The two perspectives are similar to those at $t = 4.8$: (a) is a side view similar to that in Fig. 21; (b) is a cropped plan view, similar to Fig. 22 but with the helicity brightened. A box is drawn on both panels to show where the subdomain in panel (b) has been taken from the full domain in panel (a). In panel (a) the dominant structure is the pure blue $\omega = 12$ centerline isosurface with three bridges connecting the separating upper and lower vortex rings. This illustrates what direct experimental visualizations of cores are probably observing [14]. The plan view shows what those experiments cannot see: lower ω magnitude $h \lesssim 0$ vortex sheets. Two differences with Fig. 22 are that the sheets shed from the legs change pigmentation along their length, and they are wrapping around one another at the bridges. The "left" bridge has the min(h) (red $\triangledown$) mark. The "right" bridge has the ω_m (X) and u_m (green +) marks. There is a color change on the bottom leg from orange $h < 0$ at the (X,+) "right" bridge to green at the "left" bridge. With the "left" green wrapping around the "left" bridge in the upper left and green from the leg on the right wrapping about "right" bridge and some of the y axis leg.

1. $t = 6$ isosurfaces

The last set of r1d015 isosurfaces are for $t = 6$ in Fig. 24. Instead of a finding a centerline vortex, there is a higher vorticity isosurface within the low vorticity isosurface. This figure represents when the first reconnection ends, defined as the time t_x when the $\sqrt{\nu}Z(t)$ converge in Fig. 3 and the shedding of $h < 0$ sheets has ended. The views of the isosurfaces at $t = 6$ in Fig. 24 are similar to those at $t = 4.8$ in Figs. 21 and 22: (a) a side view of the entire trefoil; and (b) a plan view of the lower ring, taken from the subdomain outlined in Fig. 24(a), with these differences.

The side view in Fig. 24(a) shows that the legs of the lower ring have separated from the upper ring, with connecting bridges whose inner, large-ω isosurfaces are winding around one another, such as in the upper right, with some wrapping of the helicity-mapped isosurface about the core. This has some similarities to how Lamb-Oseen forms upper and lower rings with connecting bridges at $t = 4$ in Fig. 19, bridges whose ends then wrap about the rings in Fig. 20. The difference is that the Lamb-Oseen bridges are transformed into isolated braids in Fig. 20, not broad vortex sheets.

What the experiments can visualize with Lagrangian markers are only the strongest isolated vortices. What those experiments miss are the low-vorticity sheets, like those at $t \geqslant 4.8$ in Fig. 22. In this sense, the algebraic large-ω bridges in Fig. 24(a), are a better representation of recent directly observed experimental vortices [14,15] than Lamb-Oseen bridges, such as in Figs. 19 and 20.

The plan view in Fig. 24(b) shows the beginnings of the next phase, with changes in the pigmentation on the sheets of the lower ring as they start wrapping around one another. The pigmentation changes from the almost all yellow, and some red, at $t = 4.8$ in Fig. 22 to pigmentation
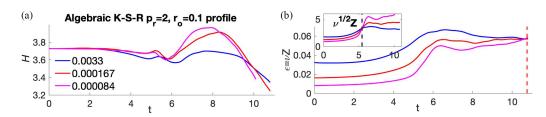
FIG. 25. Global diagnostics for case r2d1, a K-S-R algebraic profile (9) with $p_r = 2$ and $r_o = 0.1$. The figure shows the evolution of (a) helicity $\mathcal{H}$ for different viscosities and (b) two ways of scaling the enstrophy Z. The dissipation rate $\epsilon(t) = \nu Z$ with approximate convergence at $t_e = 10.75$, and in the inset convergence of the reconnection enstrophy $\sqrt{\nu}Z(t)$ at $t_x = 5.45$. These curves are similar to those for case r1d015 in Figs. 2 and 3.

at $t = 6$ in Fig. 24(b) that varies from red to yellow to green. Along the leg that runs from lower right to the upper left, there is orange ($h < 0$) coming out of the bridge in the lower right, yellow ($h \lesssim 0$) on the shed sheet in the middle, then green ($h \gtrsim 0$) on the left that is wrapping around the bridge and another sheet. This variation in color suggests that the sign for the vortical velocity $\boldsymbol{u} \cdot \hat{\omega}$ is also changing, which implies stretching along the legs.

Given that these stretched sheets are wrapping around the bridges and their neighboring sheets, a configuration has been created with all the elements required to invoke the Lundgren model [17] for stretched spiral vortices. This is the only analytic model that generates a $-5/3$ Kolmogorov-like spectra. It also provides one path for explaining the dissipation anomalies (1) indicated in Figs. 3(b) and 25(b). Work on the details of the responsible inter-sheet dynamics is in progress.

F. Reconnection-dissipation structures for K-S-R $p_r = 2$

To finish the cases, a few results from the two K-S-R $p_r = 2$ cases r2d1 and r2d05 are included. Recall that due to stability (14), these profiles are stable unless the azimuthal wave number m (13) is very large. For case r2d1, the evolution of Z, $\sqrt{\nu}Z$ and $\mathcal{H}$ mirrors that of case r1d015 in Fig. 2 so its details are not given. This includes strong convergence of $\sqrt{\nu}Z$ at the same time of $t_x \simeq 6$, and approximate convergence of the dissipation rate $\epsilon = \nu Z$ at $t_\epsilon \approx 10$, with similar post-reconnection $\mathcal{H}(t)$ growth, then decay. The evolution of its three-dimensional structures is also similar.

The calculations with thinner initial algebraic cores (r2d05 and r1d006) behave differently. Both, as in Fig. 26, generate $\sqrt{\nu}Z$ convergence, but earlier than r2d05 and r1d015, and both fail to generation dissipation rate ϵ convergence. For r2d05, the post-reconnection vortex structures in Fig. 27 have similarities with the Lamb-Oseen braids in Fig. 20.

These final results are likely due to the constraints imposed by the three-fold symmetry and the confined $(2\pi)^3$ periodic domain. It has previously been shown that if the core thickness is thinner
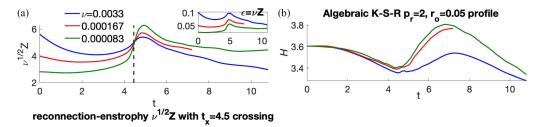

FIG. 26. Global diagnostics for case r2d05, algebraic with $p_r = 2$ and $r_o = 0.05$, for different viscosities, showing (a) convergence of $\sqrt{\nu}Z(t)$ at $t = 4.45$, but without convergence of the dissipation rate $\epsilon(t) = \nu Z$ as shown in the inset; (b) strong post-reconnection growth of the helicity $\mathcal{H}$. Case r1d006 ($p_r = 1$, $r_o = 0.006$) has similar $Z(t)$, $\sqrt{\nu}Z(t)$ and $\mathcal{H}(t)$ evolution. In the next figure, r2d05 does not develop strong $h < 0$ vortex sheets, nor does r1d006.
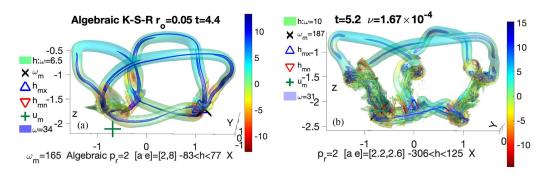
FIG. 27. Side-views of isosurfaces for algebraic case r2d05, $p_r = 2$ (9) at $t = 4.4$ and 5.2. Perspective angles and the range of the helicity density h are given at the bottom of each panel. High ω isosurfaces are used instead of vortex lines to indicate the centerlines. (a) Time $t = t_x = 4.4$ is when the $\sqrt{\nu}Z(t)$ cross in Fig. 26 and a vortex sheet is starting to form. However, $t_x = 4.4$ is earlier ($t < 5$) than in Figs. 3 and 25. (b) And at $t = 5.2$, instead of sheets continuing to form, there are connecting bridges at $t = 5.2$. The formation of bridges instead of vortex sheets is similar to Lamb-Oseen in Fig. 19, possibly because for both the outer gradients are steep. For case r1d05 this is due to the thin core radius and the influence of the restrictive $(2\pi)^3$ domain.

[1] or the Reynolds number is higher [2], larger domains are required to get convergence of $\sqrt{\nu}Z$. And that by breaking these constraints [2], the calculation can attain the accelerated enstrophy growth required for first $\sqrt{\nu}Z(t)$ convergence, then approximate convergence of the dissipation rates $\epsilon = \nu Z$ by a ν-independent time. This is not possible for the final r2d05 and r1d006 calculations due to those constraints. Full discussion of these questions using new calculations in larger domains and a wider range of viscosities will be in a paper in preparation.

IV. SUMMARY

A. Concluding remarks

The critical points in this paper are the following:

(a) Demonstrating that the evolution of the enstrophy and helicity up to and at reconnection depend significantly upon the initial vorticity profile even when vortex knots have the same initial trajectory and circulation.

(b) Introducing vortex centerline diagnostics capable of showing how the evolution from different initial profiles diverges.

(c) Explaining the structural differences that form during the first reconnection: vortex bridges/braids for the Gaussian/Lamb-Oseen profile and vortex sheets for all the algebraic profiles.

Not covered are the interactions between the vortex sheets of the widest algebraic profiles that lead to ν-independent convergence of ϵ and finite ΔE_ϵ (1). That will be the topic of another paper that extends to later times the previous calculations of perturbed trefoil knots in domains that grow as the viscosity decreases [2].

Only the two outlying cases (Gd05 and r1d015) have been discussed in detail. For each, these are the critical questions:

(1) Is it subject to either infinitesimal or finite perturbation instabilities?

(2) How does its $t = 0$ stability influence its reconnection-time behavior?

(3) And does that behavior allow finite energy dissipation to form, or not?

The answer to question (1) comes from recent mathematics [13] that shows that initial profiles can be subject to instabilities when the initial state has small, but not tiny, perturbations. If so, then the mathematics of instabilities upon a columnar vortex [12], illustrated in Fig. 6, can be used to show that for almost all wave numbers, there is a Richardson number-dependent instability (12), as in Fig. 5. This develops despite the Lamb-Oseen profile being the favorite choice of the engineering community. The resulting instability-induced proliferation of $\omega = 0$ contours is illustrated by the

$t = 1.2\ \omega_y$ cross section in Fig. 8, a property previously observed for perturbed antiparallel vortices [7,11].

In contrast, the regularized $p_r = 1$ and $p_r = 2$ algebraic profiles (9) are almost always stable, with a comparison ω_y cross section given in Fig. 7.

How can those small $t \gtrsim 0$ differences be the origin of the dramatic post-reconnection differences? New diagnostics are required because between cases, there are few differences for the enstrophy $Z(t)$ and helicity $\mathcal{H}(t)$ until reconnection truly begins.

The most that the mapped-helicity isosurfaces can tell us about the dynamics is that around regions of negative helicity $h < 0$, sometimes just spots of yellow or red, viscous reconnection develops as the nonlinear timescale of $t_r \sim 4$ is approached. What the isosurfaces cannot explain is why the new structures that are generated are so different, bridges and braids for Lamb-Oseen and isosurface sheets for all of the algebraic profiles. What is needed is a set of diagnostics that can follow the dynamics of the interiors before the enstrophy $Z(t)$ and the helicity $\mathcal{H}(t)$ diverge after $t \sim t_r$.

(2a) The terms from the enstrophy and helicity budget equations (5) and (6) are another set of diagnostics that might provide evidence for the early origins for the differences between cases. These could be mapped onto isosurfaces, as done for the helicity, or on the centerlines. When mapped onto the isosurfaces, their variations are too weak to be useful. In contrast, when mapped onto the centerline vortices (17), the variations are substantial.

(2b) The chosen centerline diagnostics in this paper are h, ϵ_h, $|\omega| = \sqrt{\zeta}$, h_f, ϵ_ζ and ζ_p, and are arranged into four panels. Plus, vertical dashed lines in every panel at positions related to local extrema. This includes the positions of local min(h_f), local min(ϵ_h) and their nearest positions on the opposite loop of the trefoil. By following and comparing their extrema between the panels and the isosurfaces, a picture of the evolution emerges.

The diagnostics that carry the most information at early times are the centerline positions of local min(h_f), h-flux minima (6). At the earliest times shown, $t = 1.2$ for r1d015 algebraic profile and $t = 0.4$ for Lamb-Oseen case Gd05, the local min(h_f) can be matched with several extrema: local minima and maxima of the helicity dissipation ϵ_h and minima of the enstrophy production ζ_p (5), as given in Figs. 9 and 10. For algebraic case r1d015, from $t = 1.2$ to when reconnection begins, the relative centerline positions of these extrema are stable, allowing the $h < 0$ zones on the new lower ring to gradually shed $h < 0$ vortex sheets.

In the period $t = 1.2-2.4$, the relative positions on the Lamb-Oseen centerline profiles are not stable. Figure 11 at $t = 1.2$ has six roughly equivalent positive and negative excursions of ϵ_h around positions of local compression, local min(ζ_p) < 0, likely due to local interactions with the instability-induced, oppositely signed patches shown in Fig. 8. Three are associated with the s_f points. The other three with their s_o opposing points.

The Lamb-Oseen s_f points return to something akin to normal for the budget curves at $t = 2.4$ in Fig. 12. However, the damage has been done and when reconnection begins at $t = 3.6$, the reconnection structures form only between the $t = 1.2$ extrema points.

(3) It is these differences in the respective $t \leqslant 2.4$ budgets that determine whether the post-reconnection structures are braids or sheets and whether finite energy dissipation can form. Post-reconnection Lamb-Oseen first generates bridges, as at $t = 4$ in Fig. 19, then progresses to braids at $t = 4.4$ in Fig. 19, with only a sort-lived growth in the enstrophy $Z(t)$ and energy dissipation $\epsilon(t)$ in Fig. 1 before Z and ϵ decay.

This contrasts with the algebraic profiles that do not have this instability, or any excessive local compression. Due to this, the helicity transport h_f is able to spread $h < 0$ along the centerline, from which $h < 0$ vortex sheets can be shed as the trefoil self-reconnects, as shown in Figs. 16 and 28 at $t = 3.6$ and Figs. 21 and 22 at $t = 4.8$. Fig. 24 at $t = 6$ shows how those sheets, when interacting, can allow the enstrophy growth to accelerate and convergent energy dissipation rates ϵ to be achieved, leading to evidence for a dissipation anomaly with finite ΔE_ϵ (1). The only evidence for bridges or braids coming from the algebraic calculations is internal higher-ω isosurfaces, as in Fig. 24, which do not contain the bulk of the enstrophy.

B. Discussion

The centerline budget diagnostics introduced here will next be applied to extensions, or variations upon, two existing calculations: first, extensions of the earlier, perturbed trefoils in very large domains [2] to higher Reynolds numbers and later times, and, second, versions of recent calculations of interacting orthogonal vortices [16]. For both, there is a phase during which the interacting vortices flatten as ν-independent convergent $\sqrt{\nu}Z$ is observed at t_x, followed by approximately convergent ν-independent dissipation rates $\epsilon = \nu Z$ that develop and form as the sheets interact with one another.

On the orthogonal isosurfaces, the mapped helicity indicates that within that wrapping, the vortex stretching is vortical, observations that are consistent with the Lundgren spiral vortex model [17] for generating a $-5/3$ energy spectrum. At the time (circa 1982), a mechanism for creating wrapped and stretched vortex sheets within a turbulent flow had not been demonstrated, although in retrospect, this is probably what stills [18] taken from the earliest color, three-dimensional animations of interacting vortices are showing.

The recent orthogonal vortices [16] were initialized with a Lamb-Oseen profile, and did not develop $t \gtrsim 0$ negatively signed ghost vortices. Based upon the recent mathematics [13] this could be because those vortex tubes were not curved, but straight, and so were not modified by the solenoidal projection as in initialization step 4 in Sec. II A. The result is that the perturbations are inherently numerical and tiny, lacking a perturbation on their outer edge similar to that in Fig. 5. That mathematical analysis [13], after stating the columnar vortex stability function $J(\rho)$ (12), says that tiny perturbations should not generate strong instabilities. That is, if a Lamb-Oseen profile is applied to straight vortex tubes, there will not be any instabilities capable of generating negatively signed ghosts like those in Fig. 8 and earlier work [7].

Other Lamb-Oseen calculations. In the recent review [19] of the state of numerical vortex reconnection, a reconnection-to-bridges to braids cascade paradigm was presented based upon the results from Lamb-Oseen profile calculations, without any examples given of a second step in that cascade. Given the contrasting enstrophy evolution of the algebraic calculations, how should that paradigm be changed?

The changes are substantial, with the algebraic alternative being a two-step process instead of a cascade.

(1) First, a period that ends at t_x with $\sqrt{\nu}Z(t)$ convergence, generation of $h < 0$ vortex sheets and completion of the first reconnection.

(2) Next, a period covering $t_x < t \lesssim t_\epsilon \approx 2t_x$ during which the sheets wrap around one another, leading to convergent $\epsilon = \nu Z$.

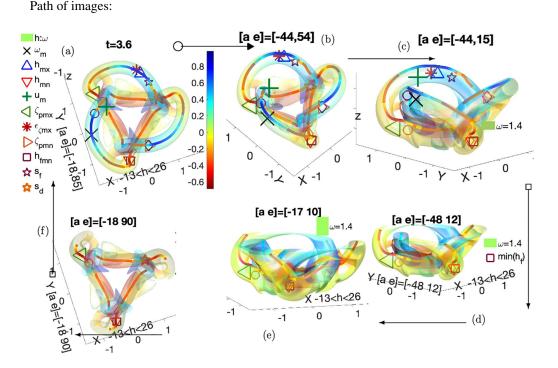Finally, As that large ϵ persists, finite-time, finite ΔE_ϵ (1) forms.

Furthermore, because that review [19] focuses upon their recent trefoil calculation [3] as the latest support for the reconnection-to-braids paradigm, it is fair to ask whether the instabilities identified here extend to all the cited Gaussian/Lamb-Oseen calculations in that review.

They probably do, going back to the first calculations in 1989 [20] that use a modified Lamb-Oseen profile. The effects of such instabilities were first clearly identified for an Euler calculation using an elongated Gaussian profile [11] and were then clarified by antiparallel analysis [7] in 2013 that shows $t \sim 0$ $\omega = 0$ contours that are more intense than those in Fig. 8. If the authors of that recent review [19] disagree with the analysis behind these conclusions, what would be useful would be a reply or comment that applies the centerline diagnostics introduced here to one of their recent calculations.

elements during the final preparation. Computing resources have been provided by the Scientific Computing Research Technology Platform at the University of Warwick.

APPENDIX: SEQUENCE OF ALGEBRAIC $t = 3.6$ ISOSURFACES

Path of images:

FIG. 28. Six views of the three-dimensional vorticity isosurface with mapped helicity at $t = 3.6$ for algebraic case r1d015 with $\nu = 8.4 \times 10^{-4}$. The legend on the left of (a) and the color bar to its right apply to all panels, with [a e] = Ω_z [rotation elevation]. In these panels, the dominant features are on or around the centerline. Starting with panel (a) where the reddish regions hugging the centerlines show where $h < 0$ is being shed. The sequence starts in upper-left with: (a) [a e] = $[-18, 85]$, as in Fig. 16(a); next is panel (b), which is rotated to [a e] = $[-44\ 43]$ to be similar to the high-ω isosurface in Fig. 15(b). Panels (c), (d) are rotated gradually into a side view, indicating where slightly negative helicity $h \lesssim 0$ sheets are appearing underneath the centerline. Panels (d)–(f) shave off, then lop off, the blue top of the trefoil, leaving its bottom half, which is dominated by shed, yellow $h \lesssim 0$ vortex sheets. These sheets have the appearance of the ruffles of a yellow skirt sticking out below the main blue $h > 0$ trefoil. To follow the rotation between panels (d), (e), use the lime bulge with the maroon $\square$ of $\min(h_f)$. Then panel (f) shows the bottom half of panel (a), providing a view of the $h < 0$ vortex sheets on the periphery, including three very faint $h \lesssim 0$ yellow lobes. These become the more extensive $h \lesssim 0$ sheets at $t = 4.8$ in Fig. 22.

[1] R. M. Kerr, Trefoil knot timescales for reconnection and helicity, Fluid Dyn. Res. **50**, 011422 (2018).
[2] R. M. Kerr, Enstrophy and circulation scaling for Navier-Stokes reconnection, J. Fluid Mech. **839**, R2 (2018).
[3] H. J. Yao, Y. Yang, and F. Hussain, Dynamics of a trefoil knotted vortex, J. Fluid Mech. **923**, A19 (2021).
[4] X. Zhao and C. Scalo, Helicity dynamics in reconnection events of topologically complex vortex flows, J. Fluid Mech. **920**, A30 (2021).
[5] A. Alexakis and L. Biferale, Cascades and transitions in turbulent flows, Phys. Rep. **767–769**, 1 (2018).
[6] L. Rosenhead, The formation of vortices from a surface of discontinuity, Proc. R. Soc. A **134**, 170 (1931).

 [7] R. M. Kerr, Fully developed hydrodynamic turbulence from a chain reaction of reconnection events, Procedia IUTAM **9**, 57 (2013).

 [8] R. M. Kerr, Swirling, turbulent vortex rings formed from a chain reaction of reconnection events, Phys. Fluids **25**, 065101 (2013).

 [9] R. M. Kerr, Topology of interacting coiled vortex rings, J. Fluid Mech. **854**, R2 (2018).

[10] H. K. Moffatt, Helicity and singular structures in fluid dynamics, Proc. Natl. Acad. Sci. USA **111**, 3663 (2014).

[11] M. D. Bustamante and R. M. Kerr, 3D Euler about a 2D symmetry plane, Physica D **237**, 1912 (2008).

[12] L. N. Howard and A. S. Gupta, On the hydrodynamic and hydromagnetic stability of swirling flows, J. Fluid Mech. **14**, 463 (1962).

[13] T. Gallay and D. Smets, Spectral stability of inviscid columnar vortices, Anal. PDE **13**, 1777 (2020).

[14] D. Kleckner and W. T. M. Irvine, Creation and dynamics of knotted vortices, Nat. Phys. **9**, 253 (2013).

[15] M. W. Scheeler, D. Kleckner, D. Proment, G. L. Kindlmann, and W. T. M. Irvine, Helicity conservation by flow across scales in reconnecting vortex links and knots, Proc. Natl. Acad. Sci. USA **111**, 15350 (2014).

[16] R. Ostilla-Mónico, R. McKeown, M. P. Brenner, S. M. Rubenstein, and A. Pumir, Cascades and reconnection in interacting vortex filaments, Phys. Rev. Fluids **6**, 074701 (2021).

[17] T. S. Lundgren, Strained spiral vortex model for turbulent fine structure, Phys. Fluids **25**, 2193 (1982).

[18] R. M. Kerr, Higher order derivative correlations and the alignment of small-scale structures in isotropic numerical turbulence, J. Fluid Mech. **153**, 31 (1985).

[19] J. Yao and F. Hussain, Vortex reconnection and turbulence cascade, Annu. Rev. Fluid Mech. **54**, 317 (2022).

[20] M. V. Melander and F. Hussain, Cross-linking of two antiparallel vortex tubes, Phys. Fluids A **1**, 633 (1989).